

23 **Abstract**

24 The co-existence of motile macroorganisms and mat-building cyanobacteria in the
25 Paleoproterozoic FB₂ Member of the Franceville sub-basin, Gabon, points to the possible
26 emergence of multi-trophic-level biological interaction by 2.1 billion years (Ga) ago. However,
27 it is uncertain how these shallow-marine communities acquired and cycled nitrogen, a key,
28 biolimiting nutrient required to sustain life at all trophic levels. Here, we use carbon and
29 nitrogen isotope data from ancient microbial mats and host sediments, in combination with
30 bottom-water redox proxies, to constrain biogeochemical processes operating in these
31 settings. In this shallow-marine upwelling zone, iron speciation data and redox-sensitive
32 metal concentrations point to oxygen-deficient bottom waters, which were episodically
33 renewed with upwelling deep anoxic waters rich in nutrients and manganese. Organic carbon
34 and nitrogen isotopes show little difference between the mat-related structures (MRS) and
35 host sediments, suggesting either that similar metabolisms operated in benthic and
36 planktonic microbial communities or that benthic carbon fixation contributed organic matter to
37 the host sediments. The isotopic fractionation between organic and inorganic carbon is as
38 large as 44‰, implying the involvement of multiple levels of heterotrophic carbon processing,
39 linked to phototrophy, secondary productivity, and methanotrophy. Whole-rock nitrogen
40 isotope values in the range of -3.5 to +1.9‰ are consistent with microbial community
41 nitrogen fixation in a nitrate-limited ecosystem. These data suggest that nitrogen fixation,
42 common in photosynthetic microbial mats in modern environments, operated in benthic
43 settings in the coastal area of the mid-Paleoproterozoic Franceville sub-basin. The upwelling
44 of deep, anoxic waters invoked for deposition of the upper part of the underlying FB₁ Member
45 suggests that basin-scale redox structure modulated nitrate availability in this otherwise oxic,
46 shallow-marine basin shelf environment.

47 **Keywords**

48 Mat-related structures, Paleoproterozoic, nitrogen isotopes, paleoredox, basinal structure,
49 Francevillian biota

50 Introduction

51 The Paleoproterozoic Era, 2.5–1.6 billion years ago (Ga), was a time of profound
52 change in atmosphere-ocean chemistry, including the so-called “Great Oxidation Event”
53 (GOE; Holland, 2002; Bekker *et al.*, 2004) that promoted the global emergence of oxidizing
54 conditions at Earth’s surface over an interval of 300 million years (Bekker and Holland, 2012;
55 Lyons *et al.*, 2014). The onset of the GOE, constrained by the disappearance of mass-
56 independent fractionation in sulfur isotopes at *ca.* 2.46-2.43 Ga (Gumsley *et al.*, 2017; Warke
57 *et al.*, 2020), records a rise in atmospheric oxygen above 10^{-5} times present atmospheric
58 level (Farquhar *et al.*, 2001; Pavlov and Kasting, 2002). Evidence for oxygenated surface
59 environments comes from sedimentary and geochemical proxies including the
60 disappearance of redox-sensitive detrital minerals, the appearance of red beds and sulfate
61 evaporites, and enrichment of redox-sensitive trace elements in iron formations and organic-
62 rich shales (Bankole *et al.*, 2016; Bekker *et al.*, 2006; Chi Fru *et al.*, 2019, 2016; Kipp *et al.*,
63 2017; Konhauser *et al.*, 2011; Melezhik *et al.*, 2005; Partin *et al.*, 2013; Rasmussen and
64 Buick, 1999; Schröder *et al.*, 2008; Scott *et al.*, 2008).

65 The redox-sensitivity of the biogeochemical cycle of nitrogen (N) - an essential
66 nutrient needed for the construction of biomolecules in all known living organisms - has
67 resulted in dramatic redox transformation of the N cycle as the redox state of the Earth’s
68 surface evolved through time (Stüeken *et al.*, 2016). The primary source of nitrogen to the
69 biosphere is assimilation of dinitrogen (N_2) into biomass by nitrogen-fixing organisms
70 (diazotrophs). In oxygen-depleted settings, biologically mediated degradation of diazotrophic
71 biomass produces bioavailable ammonium (NH_4^+). In oxygen-rich waters, NH_4^+ is rapidly
72 oxidized to nitrite (NO_2^-) and nitrate (NO_3^-) via the stepwise process of bacterial nitrification.
73 These bioavailable N forms can be assimilated directly or returned to the atmosphere as N_2
74 via denitrification (*i.e.*, reduction of NO_3^- to N_2) and anaerobic ammonium oxidation
75 (anammox; NH_4^+ oxidation coupled to NO_2^- reduction). These microbial N removal pathways
76 are prevalent in modern oxygen-minimum zones (Dalsgaard *et al.*, 2005; Sigman *et al.*,
77 2009), meaning that oxygen-deficient waters are likely to become depleted in dissolved N.
78 Thus, studying the response of the N cycle to Earth’s oxygenation can not only yield more
79 precise constraints on water column redox conditions, but also can be informative about N
80 availability for early marine ecosystems.

81 Because the stable isotopes of N are fractionated during the redox transformations
82 mentioned above, many studies leverage N isotope ratios in ancient marine sedimentary
83 rocks as a means to study the N cycle in deep time (reviewed in Ader *et al.*, 2016). This
84 includes recent studies that have used N isotopes to infer that aerobic N cycling emerged in

85 a stepwise fashion during the GOE (Cheng et al., 2019; Kump et al., 2011; Luo et al., 2018;
86 Zerkle et al., 2017) and was pervasive in the surface oceans during much of the
87 Paleoproterozoic (Kipp et al., 2018). These studies focused on the global-scale evolution of
88 the marine N cycle across the GOE; however, the basin-scale impact of redox fluctuations,
89 linked to extant N fixing and assimilating communities, as well as episodic incursions of
90 anoxic deep waters, has not yet been studied for the late stage or the immediate aftermath of
91 the GOE. Here, we explore N redox dynamics in the middle Paleoproterozoic Franceville
92 sub-basin of Gabon with a particular focus on a sedimentary interval that bears large
93 microfossils and microbial mat-related structures (MRS). This allowed us to explore the
94 relationships among redox structure, nutrient cycling, and the early evolution of complex life
95 in this pivotal interval.

96 The timing of deposition in the Franceville sub-basin corresponds in age to the end of
97 the Lomagundi Event (LE) (~2.22–2.06 Ga; Karhu & Holland, 1996; Canfield *et al.*, 2013).
98 This event represents the longest-lived positive carbon isotope excursion in Earth’s history,
99 during which atmospheric oxygen levels rose considerably (Bekker and Holland, 2012;
100 Planavsky et al., 2012). The *ca.* 2.1 Ga Franceville sub-basin records frequent eustatic
101 changes and episodic upwelling of deep, anoxic waters into shallow-marine, oxic settings
102 (Gauthier-Lafaye and Weber, 2003; Ossa Ossa et al., 2018; Reynaud et al., 2017) that could
103 have influenced the spatiotemporal dynamics of the N cycle. As only one stratigraphic unit of
104 the Francevillian Group (FC₁ Member) has been the focus of N isotope study so far (Kipp et
105 al., 2018), there remains a considerable gap in our understanding of N cycling throughout the
106 whole Francevillian Group sedimentary record. Furthermore, the Francevillian Group
107 sedimentary rocks have revealed tantalizing evidence that the earliest potential multicellular
108 life (El Albani et al., 2014, 2010) capable of locomotion (El Albani et al., 2019) flourished next
109 to benthic microbial mats (Aubineau et al., 2018; El Albani et al., 2019; Reynaud et al.,
110 2017). The microbial features, preserved as MRS, display a wide range of surface
111 morphologies with mat-growth and mat-protected patterns. The former, including “elephant-
112 skin” textures (EST), domal buildups, and discoidal microbial colonies, consist of the mat
113 layer itself generated through mat propagation, while the latter, such as wrinkle and
114 “*Kinneyia*” structures, arose from structures that relied on the mat communities for their
115 preservation/protection. Individual MRS vary between 0.2 and 3 mm in thickness; this
116 heterogeneity has been attributed to changes in physical and chemical environmental factors
117 (Aubineau et al., 2020). According to their sulfur content (0.15 to 29.37 wt. %), the
118 Francevillian MRS are further divided into unpyritized EST (0.15 to 0.36 wt. %), poorly
119 pyritized MRS (0.19 to 4.16 wt. %), and pyritized MRS (6.46 to 29.37 wt. %) (cf. Aubineau et

120 al., 2020). Detailed descriptions of textural diversity and elemental geochemistry of MRS are
121 provided in Aubineau et al. (2020, 2018).

122 Morphological and microtextural observations have shown that the MRS were likely
123 dominated by cyanobacterial communities (Aubineau et al., 2019, 2018). In modern
124 environments, similar microbial mat communities are capable of “fixing” atmospheric nitrogen
125 into bioavailable nitrogen that is subsequently utilized by microorganisms (Bebout et al.,
126 1994; Herbert, 1999). Nitrogen fixation fulfills the N requirement for primary production, thus
127 sustaining mat growth. Cyanobacterial mats exhibit high annual N fixation activity in the
128 range of 0.8 to 76 g N m⁻² year⁻¹, fueling high rates of CO₂ reduction during photosynthesis
129 (Herbert, 1999; Woebken et al., 2015). This bioavailable nitrogen produced by diazotrophs is
130 entirely consumed by the wide array of microorganisms existing within the mat (Bebout et al.,
131 1994). Hence, the Francevillian Group mats could show a similar pattern of N cycling as
132 there is no *a priori* reason to believe that Precambrian mats behaved differently from their
133 modern counterparts.

134 In order to provide further insight into N cycling and microbial biogeochemistry at the
135 end of the LE, this study focused on the MRS and their associated host sediments of the
136 Francevillian Group FB₂ Member. Both have been previously characterized for their
137 mineralogy and elemental composition (Aubineau et al., 2020, 2019). Here, we use iron-
138 based redox analyses and redox-sensitive element concentrations to constrain local redox
139 conditions in the depositional setting. We additionally measured organic carbon ($\delta^{13}\text{C}_{\text{org}}$) and
140 whole-rock plus kerogen-bound nitrogen ($\delta^{15}\text{N}$) isotope compositions of both the microbial
141 structures and host rocks to highlight potential differences related to microbial ecology (*i.e.*,
142 benthic vs. planktonic communities) among the diverse lithologies. In conjunction with
143 previously published data (Kipp et al., 2018; Ossa Ossa et al., 2018), we explore the spatial
144 and temporal trends in C and N isotope records of the Upper Francevillian Group to constrain
145 the basin-scale trajectory of C and N cycling at the end of the LE, and implications for the
146 unique microfossil record of the Franceville sub-basin.

147 **Geological setting**

148 The Francevillian Group in southeastern Gabon comprises five sedimentary formations (FA
149 to FE) deposited during the middle Paleoproterozoic (Fig. 1a). This 1.0 to 2.5 km-thick
150 sedimentary succession rests unconformably on the Archean crystalline basement (Fig. 1b;
151 Weber, 1968). The basal FA Formation, consisting mainly of fluvial to fluvio-deltaic
152 sandstones accumulated during a progressive basin opening to marine conditions (Bankole
153 et al., 2015; Gauthier-Lafaye and Weber, 1989), is widely known for post-depositional

154 uranium ore deposits hosted in the Upper FA Formation (Bankole et al., 2016; Gauthier-
155 Lafaye and Weber, 2003, 1989). After a period of tectonic subsidence and deepening in the
156 foreland basin (cf. Bankole et al., 2018; Ossa Ossa et al., 2020), the FA formation gave way
157 to a predominantly marine depositional phase, starting with the FB Formation. The latter is
158 lithostratigraphically subdivided into FB₁ (including a, b, and c units) and FB₂ (a and b units)
159 members (Azziley Azzibrouck, 1986; Weber, 1968).

160 The FB_{1a} unit consists entirely of green shales, while the FB_{1b} unit contains both black
161 shales and heterolithic beds, with the latter characterized by rhythmic couplets of greyish
162 shale and dolomite-cemented siltstones (Reynaud et al., 2017). Following an episode of sea
163 level rise, deposition continued with the FB_{1c} unit characterized by black shales, the upper
164 part of which contains iron- and manganese-rich sediments (Gauthier-Lafaye and Weber,
165 2003). Episodic submarine volcanism and hydrothermal activity have been inferred as the
166 potential sources of aqueous Fe(II) and Mn(II), transported from deep anoxic settings onto
167 the basin margin by upwelling to form the Fe and Mn deposits (Ossa Ossa et al., 2018).
168 These upwelling events brought reductants and nutrients onto the oxic, shallow-marine basin
169 shelf (Gauthier-Lafaye and Weber, 2003), which would have driven oxygen consumption,
170 contributing to the first of two steps in seawater deoxygenation in the Franceville sub-basin at
171 the end of the LE (Ossa Ossa et al., 2018).

172 The FB_{2a} unit, formed during sea level fall (Reynaud et al., 2017), is characterized by
173 massive sandstones with black shale interbeds and overlain by laminated black shales of the
174 FB_{2b} unit, frequently intercalated with cm-thick siltstone layers. The FB₂ Member was
175 deposited in a mud-dominated setting with high-density sand flows (Reynaud et al., 2017).
176 The multiple sulfur isotope composition of authigenic pyrite in these units indicates that the
177 seawater column during their deposition was relatively oxygenated with a sizable sulfate
178 reservoir (Canfield et al., 2013; El Albani et al., 2019; Ossa Ossa et al., 2018). In addition,
179 the black shales of the FB_{2b} unit host well-preserved complex macrofossils and delicate MRS
180 (Aubineau et al., 2018; El Albani et al., 2019, 2014, 2010).

181 The overlying FC Formation, deposited mainly in a tidal-flat setting, is further divided
182 into the FC₁ and FC₂ members based on lithological composition (Ossa Ossa et al., 2018).
183 The Lower FC Formation consists of massive dolostones and black shales (Préat et al.,
184 2011; Weber, 1968) with manganese-rich sediments at the top (Ossa Ossa et al., 2018),
185 while the Upper FC Formation is dominated by stromatolitic chert associated with the oldest
186 Gunflint-type assemblage of microfossils that includes filamentous cyanobacteria (Bertrand-
187 Sarfati and Potin, 1994; Lekele Baghekema et al., 2017). The FD Formation contains marine
188 fine- to medium-grained sedimentary rocks alternating with volcanic tuffs (Thiéblemont et al.,

189 2014), above which the sandstones of the FE Formation were deposited (Gauthier-Lafaye
190 and Weber, 1989; Thiéblemont et al., 2014).

191 Although the depositional age is still controversial and poorly resolved (Fig. 1b) (e.g.,
192 Bros et al., 1992), precise U-Pb zircon ages of 2083 ± 6 Ma and 2072 ± 29 Ma were reported
193 from ignimbrite tuffs and sandstones near the top of the FD Formation, respectively (Horie et
194 al., 2005; Thiéblemont et al., 2009). Based on the falling limb of the large-magnitude positive
195 excursion in $\delta^{13}\text{C}$ recorded in marine carbonates ($\delta^{13}\text{C}_{\text{carb}}$) of the FB and lower FC
196 formations, these units are thought to have been deposited at the end of the LE (Canfield et
197 al., 2013; El Albani et al., 2010; Ossa Ossa et al., 2018; Pr eat et al., 2011). The similar end
198 to the positive $\delta^{13}\text{C}_{\text{carb}}$ excursion observed in the lowermost part of the ca. 2.0 Ga Zaonega
199 Formation (ZF; Karelia Craton, NW Russia; Hannah et al., 2008; Martin et al., 2015),
200 together with similar large negative excursions large in $\delta^{13}\text{C}_{\text{org}}$ values below 40‰ in both the
201 FD Formation and ZF, have led to the interpretation that these formations might have been
202 deposited contemporaneously (Canfield et al., 2013; Kump et al., 2011). Therefore,
203 deposition of both the FD Formation and ZF most likely corresponds to the aftermath of the
204 LE.

205 A different view was recently presented by (Mayika et al., 2020), who argued that
206 carbon isotope composition of marine carbonates in the Franceville sub-basin reflects
207 basinal stratification with waters in shallow-marine settings having highly positive C isotope
208 values, while waters in deep-marine settings having near-to-zero C isotope values with the
209 difference approaching 10‰. Mayika *et al.* (2020) related highly positive C isotope values in
210 shallow-water carbonates in the Franceville sub-basin to either high degree of evaporation or
211 high primary productivity in these settings. In other words, this study speculated that the
212 carbon cycle variations in the Franceville sub-basin reflect only regional, basin-scale
213 conditions. However, this extreme level of C-isotope fractionation between shallow and deep
214 waters and deposits is not observed in modern or ancient open-marine settings nor predicted
215 on the theoretical grounds for the Paleoproterozoic $p\text{CO}_2$ (Bjerrum and Canfield, 2004;
216 Hotinski et al., 2004; Kroopnick, 1985, 1974). In contrast, modern, stratified basins with
217 restricted communication with the ocean (e.g., Black Sea and Kyllaren Fjord) develop similar
218 gradients, but with highly negative C isotope values in deep waters, rather than highly
219 positive C isotope values in shallow-water settings (Fry et al., 1991; Smittenberg et al.,
220 2004). Mayika *et al.* (2020) related highly positive C isotope values in shallow-water
221 carbonates in the Franceville sub-basin to either high degree of evaporation or high primary
222 productivity in these settings. The FC Member also does not show extensive development of
223 evaporites (Bouton et al., 2009a) nor does it show any evidence for enhanced productivity
224 (such as a signal of nitrogen fixation; e.g., Kipp *et al.* (2018). In contrast, mid-Proterozoic

225 carbonate successions with a strong evaporite signal or a signal for enhanced primary
226 productivity do not show high ^{13}C -enrichments (Kah et al., 2001; Papineau et al., 2009).
227 Furthermore, in the case of the Mayika *et al.* (2020) study, carbon isotope values started to
228 decrease ~10 meters below the transgressive surface, which is inconsistent with the
229 proposed basinal stratification and agrees with a global, secular control. We thus favor the
230 view that the FC Formation records the end of the LE at ca. 2.11-2.06 Ga (see Bekker et al.
231 (2021) for further discussion of Mayika et al. (2020)).

232 **Methods**

233 **Sampling.** All of our samples (both MRS and host sediments) came from outcrops in the
234 Moulendé Quarry (Fig. 1a). Before collecting outcrop material, the weathered outermost
235 surfaces were removed. We carefully separated the mat laminae from its host rock material
236 with a stainless steel razor blade – avoiding as much as possible contamination – for
237 geochemical analyses. The host sediments were sampled directly below the MRS with a
238 hammer. We made a special effort to exclude contribution of MRS to the host rocks during
239 sample preparation. We cannot entirely rule out small contribution of the underlying sediment
240 to sampled MRS, however, our sampling procedure did not result in significant contamination
241 as far as distinct clay minerals and geochemical compositions were observed for samples of
242 the MRS and their host sediments (Aubineau et al., 2020, 2019).

243 **Scanning electron microscopy.** Pyrite morphology of MRS and black shales was studied in
244 carbon-coated and polished slab sections, using a FEI Quanta 200 scanning electron
245 microscope (SEM) equipped with an energy-dispersive X-Ray Spectrometer (EDX) at the
246 University of Lille. The images of pyrite texture were acquired in back-scattered electron
247 (BSE) mode operated at accelerating voltage of 15 kV, 1 nA beam current, and a working
248 distance of 10.5 mm. Pyrite was specifically targeted for textural analysis to evaluate its
249 morphology and preservation, as it can be readily affected by oxidative weathering.

250 **Whole-rock analysis.** Major and trace element concentrations in powdered samples were
251 analyzed by inductively coupled plasma optical emission spectrometry (ICP-OES) and
252 inductively coupled plasma mass spectrometry (ICP-MS) at *Service d'Analyse des Roches et*
253 *Minéraux* (SARM) of the *Centre de Recherches Pétrographiques et Géochimiques* (CRPG),
254 Nancy, France. The extended protocol for major and trace element measurements at SARM-
255 CRPG is described by Carignan *et al.* (2001). Specifically, powdered samples were
256 decomposed using alkali fusion. They were fused with 900 mg of ultra-pure lithium
257 metaborate at 980°C to form a glass. Then, the glass was dissolved in a mixture of 1 M nitric
258 acid, 0.5% hydrogen peroxide, and 10% glycerol. The uncertainty for major elements was

259 determined to be better than 5%, with the exception of Ca (10%) and P (>25%), while that for
260 trace elements was lower than 5% for concentrations >10 ppm and 15% for concentrations
261 between 10 and 1 ppm and >25% for elemental concentrations near the detection limit, as
262 checked with international standards and analysis of replicate samples (cf. Carignan *et al.*,
263 2001).

264 Enrichment factors (EF) were calculated for Mn, P, Co, Cu, Mo, Ni, U, and V following
265 the approach described by Tribovillard *et al.* (2006). EF represents the trace metal (TM)
266 excess in the sediments, which is assessed by dividing TM/Al or TM/Ti ratios by that for the
267 upper crustal average (Rudnick and Gao, 2003). We present in Table S1 ratios of P/Ti and
268 P/Al as detrital tracers for P, following previous studies (*e.g.*, Filippelli *et al.*, 2007, 2003;
269 Latimer and Filippelli, 2001; Tribovillard *et al.*, 2006)

270 **Iron speciation analysis.** Iron speciation analysis was performed at Cardiff University,
271 according to the method of Poulton and Canfield (2005), which is reviewed elsewhere
272 (Poulton and Canfield, 2011; Raiswell *et al.*, 2018). This method targets iron that is “highly
273 reactive” (Fe_{HR}) towards hydrogen sulfide in the form of (oxyhydr)oxides (Fe_{Mag} and Fe_{Ox}),
274 carbonates (Fe_{carb}), and pyrite iron (Fe_{py}) relative to total iron (Fe_T), including poorly reactive
275 Fe (Fe_{PRS}) and unreactive Fe (Fe_U). First, Fe_{carb} was extracted with a sodium acetate buffer
276 at pH 4.5 and 50°C for 48 hours, followed by Fe_{Ox} extraction using sodium dithionite at pH
277 4.8 and room temperature for 2 hours, and finally Fe_{Mag} extraction using ammonium oxalate
278 at pH 3.2 and room temperature for 6 hours. Fe_{PRS} was then determined by boiling in 12 M
279 HCl for 2 minutes. Fe_{py} was measured by weighing a CuS precipitate after HCl and
280 chromous chloride distillation, with Fe calculated assuming FeS_2 stoichiometry (Canfield *et al.*,
281 1986). Replicate analyses between runs ($n = 5$) gave an average standard deviation of
282 0.11 wt.% for Fe_{carb} , 0.19 wt.% for Fe_{Ox} , 0.004 wt.% for Fe_{Mag} , 0.07 wt.% for Fe_{PRS} , and 0.06
283 wt.% for Fe_{py} . Samples containing <0.5 wt.% Fe were excluded from the iron speciation
284 analysis. This threshold is recommended to avoid samples that are at the resolution limit of
285 the iron-based redox proxy (see Clarkson *et al.*, 2014; Raiswell *et al.*, 2018 for reviews).

286 **Kerogen extraction.** Kerogen was isolated from selected whole-rock powders ($n = 10$) at the
287 University of Washington using the published protocol from Kipp *et al.* (2018). In brief,
288 sample powders were treated with a 1:1 mixture of concentrated HF and DI- H_2O in order to
289 dissolve silicate minerals. The resulting solutions were centrifuged and the supernatant was
290 decanted. Residual fluoride minerals were then dissolved with a BF_3 solution, and the
291 supernatant decanted after centrifugation. The remaining kerogen was then rinsed with three
292 iterations of DI- H_2O , and finally placed into a freeze-drier to remove all moisture prior to
293 analysis.

294 **Carbon and nitrogen isotope analyses.** Carbon isotope ratios for organic matter ($\delta^{13}\text{C}_{\text{org}}$)
295 and whole-rock N isotope values ($\delta^{15}\text{N}_{\text{WR}}$) were analyzed for all lithologies ($n = 34$). The
296 isotope data were measured by flash combustion on a Thermo Scientific DELTA V
297 Advantage isotope ratio mass spectrometer (IRMS), operated under a continuous helium
298 flow, and coupled to a COSTECH 4010 elemental analyzer (EA) at the University of
299 California, Riverside. For $\delta^{13}\text{C}_{\text{org}}$ analysis, ~ 200 mg of whole-rock powders were
300 decarbonized with 6 N HCl for one hour at 70°C . The solid residue was thoroughly rinsed in
301 deionized water and dried in a clean hood overnight. Small aliquots of decarbonated
302 residues (mostly less than 10 mg) were weighed into tin cups. For $\delta^{15}\text{N}_{\text{WR}}$ analysis, 20 to 50
303 mg of powdered whole-rock samples were weighed into tin cups with a blank placed after
304 each sample. Combustion at 1020° utilized ~ 10 mL of O_2 . All isotope data are reported in
305 standard δ -notation relative to V-PDB and Air- N_2 for $\delta^{13}\text{C}$ and $\delta^{15}\text{N}$, respectively. The isotope
306 measurements were standardized against three in-house standards: Acetanilide from two
307 different batches ($\delta^{13}\text{C} = -27.9\text{‰}$, $\delta^{15}\text{N} = -0.8\text{‰}$ and $\delta^{13}\text{C} = -33.7\text{‰}$, $\delta^{15}\text{N} = -0.8\text{‰}$) and
308 Hawaiian Glycine ($\delta^{13}\text{C} = -36.6\text{‰}$, $\delta^{15}\text{N} = 11.3\text{‰}$), which were calibrated to international
309 reference materials SDO-1 ($\delta^{13}\text{C} = -30.0\text{‰}$, $\delta^{15}\text{N} = -0.8\text{‰}$; Dennen *et al.*, 2006) and SGR
310 ($\delta^{13}\text{C} = -29.3\text{‰}$, $\delta^{15}\text{N} = 17.4\text{‰}$; Dennen *et al.*, 2006). Our samples are fully bracketed by the
311 isotopic compositions of the standards (Fig. S1). Replicate analyses for $\delta^{13}\text{C}_{\text{org}}$ ($n = 15$) and
312 $\delta^{15}\text{N}_{\text{WR}}$ ($n = 22$) yielded an average standard deviation (1σ) better than 0.13 and 0.15‰,
313 respectively. Total organic carbon (TOC) and total nitrogen (TN) abundances were
314 calculated from CO_2 and N_2 peak areas, respectively. The $\delta^{15}\text{N}_{\text{WR}}$ values are reported only
315 for samples with TN concentrations well above the detection limit. Atomic C:N ratios were
316 calculated by dividing mass ratios (wt.%) by molar masses of 12.01 g/mol for carbon and
317 14.01 g/mol for nitrogen such that: $\text{C:N}_{\text{WR}} (\text{atomic}) = (\text{wt.}\% \text{C}/12.01)/(\text{wt.}\% \text{N}/14.01)$.

318 For $\delta^{15}\text{N}_{\text{kerogen}}$ analysis, a few mg of kerogen were weighed into tin cups and analyzed
319 on a Costech ECS 4010 Elemental Analyzer coupled to a ThermoFinnigan MAT 253
320 continuous-flow isotope ratio mass spectrometer housed in IsoLab at the Department of
321 Earth & Space Sciences, University of Washington. Combustion utilized 20 mL of O_2 at
322 1000°C . Analytical blanks were measured and subtracted from data. The resulting isotope
323 data were standardized using in-house standards "GA1" (glutamic acid, $\delta^{15}\text{N} = -4.6\text{‰}$), "GA2"
324 (glutamic acid, $\delta^{15}\text{N} = -5.7\text{‰}$), and "SA" (dried salmon, $\delta^{15}\text{N} = +11.3\text{‰}$) that were calibrated
325 to international reference materials USGS40 and USGS41. The precision and accuracy of
326 $\text{N}_{\text{kerogen}}$ isotope analysis were better than 0.2‰, based on replicate runs ($n = 10$).

327 **Results**

328 **Redox reconstruction**

329 Iron speciation analysis of shale lithofacies is one of the most widely used methods to
330 evaluate local modern and ancient water-column redox conditions (Chi Fru et al., 2018;
331 Planavsky et al., 2011; Poulton and Canfield, 2011; Poulton and Raiswell, 2002; Sperling et
332 al., 2013). However, formation of iron monosulfides (AVS, pyrrhotite) from pyrite or a
333 conversion of unsulfidized Fe_{HR} to Fe_{PRS} during sediment diagenesis and metamorphic
334 reactions can significantly alter Fe speciation data (Slotznick et al., 2018). Iron sulfides in the
335 Francevillian Group MRS and host sediments are predominantly primary pyrite (Aubineau et
336 al., 2019). The studied samples possess mean Fe_{PRS}/Fe_T ratios of 0.07 ± 0.01 wt.% (Table
337 S2), which is below the average Paleozoic shales (0.39 ± 0.11 wt%; Raiswell *et al.*, 2008).
338 Combined, these data suggest that diagenetic and metamorphic effects are unlikely to have
339 biased our iron speciation results. Petrographic examinations also revealed that the sulfide-
340 bearing sedimentary beds in the FB₂ Member lacked an oxidized iron residue, which is
341 common to weathered horizons (cf. Aubineau *et al.*, 2018, 2020; Fig. 2). Our observations
342 thus suggest that Fe speciation systematics were not appreciably compromised by
343 secondary oxidative weathering, thermal breakdown of pyrite, or late diagenetic processes.

344 Sediments deposited under anoxic conditions are typically characterized by Fe_{HR}/Fe_T
345 ratios >0.38 , while Fe_{HR}/Fe_T ratios less than 0.22 are typical for sediments deposited under
346 oxic conditions. Values between 0.22 and 0.38 are equivocal for interpretation of local redox
347 conditions as they could reflect depositional conditions when sedimentation rate was high or
348 when the transfer of unsulfidized Fe_{HR} to less reactive clay minerals occurred during early to
349 late diagenesis (Poulton et al., 2010). Both mechanisms may mask Fe enrichment under
350 anoxic water-column conditions. If reactive Fe exceeds 38% of the Fe_T and if the Fe_{Py}/Fe_{HR}
351 values are below 0.7-0.8, deposition in ferruginous environment is inferred (Poulton and
352 Canfield, 2011). Values for $Fe_{Py}/Fe_{HR} \geq 0.7-0.8$ typically indicate sulfide-rich (euxinic) water-
353 column conditions. In addition, the Fe_T/Al proxy can also identify Fe enrichments that
354 discriminate between oxic and anoxic depositional environments (Clarkson et al., 2014;
355 Lyons and Severmann, 2006). This ratio is not affected by a transfer of unsulfidized Fe_{HR} to
356 Fe_{PRS} during diagenesis or metamorphism, meaning that the paired use of Fe_T/Al and iron
357 speciation can robustly identify primary redox conditions (Partin et al., 2015; Raiswell et al.,
358 2018). Modern marine sediments deposited under oxic conditions have Fe_T/Al ratio below
359 that of the average upper continental crust (0.55 ± 0.11), and this value can be applied as a
360 threshold for redox evaluation of siliciclastic rocks (Clarkson et al., 2014). Thus, Fe_T/Al
361 values >0.66 (with a confidence threshold of 1σ) suggest local Fe enrichments either under
362 anoxic conditions or due to hydrothermal Fe input. Strong Fe enrichments ($Fe_T/Al > 2$) are
363 often derived from an input of hydrothermal fluids to the water column (Raiswell et al., 2018).

364 The poorly pyritized and EST samples are predominantly characterized by sub-crustal
365 Fe_T/Al and low Fe_{Py}/Fe_{HR} ratios, with an upsection increase in Fe_{HR} (Fig. 3; Tables S1, S2). In
366 contrast, the pyritized MRS have supra-crustal Fe_T/Al ratios, and high Fe_{HR}/Fe_T and
367 Fe_{Py}/Fe_{HR} values. Both host sandstones and black shales have low Fe_T/Al ratios, whereas
368 the black shales show Fe_{HR}/Fe_T ratios covering the full range of redox conditions, but
369 Fe_{Py}/Fe_{HR} ratios <0.7 . The absence of significant, positive Eu anomalies in REE composition
370 of the MRS and black shales indicates that hydrothermal circulation has not strongly affected
371 the depositional site (Aubineau et al., 2020). Instead, variable redox conditions, including
372 oxic, ferruginous, and euxinic, developed during deposition of the MRS and black shales are
373 consistent with localized expression of dissimilatory iron reduction (DIR) and microbial sulfate
374 reduction (MSR) during early diagenesis (Aubineau et al., 2019, 2018) and indicate
375 deposition close to a fluctuating redoxcline.

376 **Redox-sensitive metals**

377 The average Mn concentration in the Francevillian Group FB_2 Member is 0.26 wt.% (Fig. 4,
378 Table S1), more than three times the Mn content of 0.078 wt.% in the upper continental crust
379 (UCC; Rudnick & Gao, 2003). The Mn/Al ratios and EF_{Mn} in both the MRS and host
380 sediments moderately increase upsection (Fig. 4; Table S1). On the other hand, the U/Al,
381 V/Al, and Mo/Al ratios are low for most samples, with values being even lower than those for
382 the UCC. Specifically, the redox-sensitive elements are consistently depleted relative to the
383 UCC in the FB_2 Member host sediments, with the exception of one sandstone sample (mean
384 $EF_{Mo} = 0.7 \pm 0.2$; EF_U and $EF_V = 0.4 \pm 0.1$). The pyrite-bearing MRS display enrichment in
385 Mo due to microbially induced sulfidic conditions that enhanced incorporation of chalcophilic
386 elements (Aubineau et al., 2020).

387 In the black shale samples, some elements that are known to be associated with
388 organic matter (e.g., Co, Cu, and Ni; Tribouillard *et al.*, 2006) do not show high enrichment
389 relative to the UCC (Table S1). Cobalt is moderately depleted (mean $EF_{Co} = 0.6 \pm 0.8$), while
390 Cu and Ni show only slight mean enrichments ($EF_{Cu} = 1.6 \pm 0.5$; $EF_{Ni} = 1.0 \pm 0.6$,
391 respectively).

392 **Carbon and nitrogen isotope systematics, and phosphorus enrichment**

393 The studied stratigraphic interval shows $\delta^{13}C_{org}$ values similar to the previously published
394 data for the FB_2 Member (Canfield et al., 2013; Gauthier-Lafaye and Weber, 2003), but our
395 whole-rock $\delta^{15}N$ values (Fig. 3; Table S3) differ from those recently reported for the overlying
396 FC Formation by Kipp *et al.* (2018). The average TOC content is 0.28 wt.% for sandstones
397 and 2.21 wt.% for black shales. The TN content for sandstones is close to the detection limit
398 (~ 0.01 wt.%) and thus must be treated with caution, while that for black shales is nearly

399 constant, with an average of 0.07 wt.%. This difference is accompanied by a change in mean
400 $\delta^{13}\text{C}_{\text{org}}$ values that average $-31.5 \pm 1.2\text{‰}$ (1σ , $n = 6$) for sandstones and $-35.1 \pm 0.8\text{‰}$ (1σ , n
401 $= 9$) for black shales. Thus, the transition from the FB_{2a} to FB_{2b} unit is marked by a shift
402 towards more negative $\delta^{13}\text{C}_{\text{org}}$ values. The mean $\delta^{15}\text{N}_{\text{WR}}$ value for the fine-grained sediments
403 is $-0.2 \pm 0.4\text{‰}$ (1σ , $n = 8$; ranging from -0.8 to 0.6‰), and lacks a distinct stratigraphic trend.
404 Finally, the mean $\delta^{15}\text{N}_{\text{kerogen}}$ value for the black shales is $1.4 \pm 1.0\text{‰}$ (1σ , $n = 5$; ranging from -
405 0.2 to $+2.3\text{‰}$).

406 Carbon and nitrogen contents and isotope values of the different MRS (Fig. 3, Fig.
407 S2; Table S3) reveal that TOC content is high in the poorly pyritized MRS and EST,
408 averaging 6.85 wt.% and 9.78 wt.%, respectively, and decreases, by up to 11 times, to below
409 0.87 wt.% in the pyritized MRS. Uniform mean TN values of 0.13 and 0.12 wt.% characterize
410 the poorly pyritized MRS and EST, respectively, but TN content of the pyritized MRS is twice
411 lower, with a mean of 0.06 wt.%. The $\delta^{13}\text{C}_{\text{org}}$ values average $-33.9 \pm 0.9\text{‰}$ (1σ , $n = 9$), $-30.5 \pm$
412 0.4‰ (1σ , $n = 3$), and $-33.7 \pm 0.5\text{‰}$ (1σ , $n = 7$) for the poorly pyritized MRS, EST, and
413 pyritized MRS, respectively. The mean $\delta^{13}\text{C}_{\text{org}}$ values differ between the EST and the pyrite-
414 containing MRS (*i.e.*, poorly pyritized and pyritized MRS) by up to 3.4‰, but without a
415 representative sample size, the significance level of this isotopic heterogeneity remains
416 uncertain. The MRS samples are marked by similar mean $\delta^{15}\text{N}_{\text{WR}}$ compositions of $0.8 \pm 0.6\text{‰}$
417 (1σ , $n = 9$; ranging from -0.1 to $+1.9\text{‰}$), $-1.2 \pm 2.0\text{‰}$ (1σ , $n = 3$; ranging from -3.5 to $+0.3\text{‰}$),
418 and $-1.5 \pm 1.4\text{‰}$ (1σ , $n = 5$; ranging from -3.3 to $+0.3\text{‰}$) for the poorly pyritized MRS, EST,
419 and pyritized MRS, respectively. The $\delta^{15}\text{N}_{\text{kerogen}}$ values average $2.3 \pm 1.0\text{‰}$ (1σ , $n = 5$;
420 ranging from $+0.9$ to $+3.6\text{‰}$) for the pyrite-poor MRS.

421 The section is characterized by mean P/Ti ratios (ppm/wt.%) of 0.16 and 0.31 for non-
422 pyritized MRS and black shales, respectively (Fig. 3; Table S1). Notably, P is slightly
423 enriched in the FB_{2b} unit (mean $\text{EF}_{\text{P}} = 1.8 \pm 0.2$) relative to the UCC.

424 Discussion

425 Ocean chemistry during deposition of the Francevillian Group FB₂ Member

426 To evaluate the redox state of ancient seawater robustly, Fe-based redox proxies should be
427 coupled with other available redox proxies. The sedimentary enrichment of redox-sensitive
428 trace metals is one source of such information, with the potential to reconstruct bottom-water
429 redox conditions. For example, enrichments in U and V preferentially occur under anoxic
430 (euxinic and ferruginous) conditions, while Mo is readily scavenged in anoxic, sulfide-rich
431 (euxinic) waters (Scott et al., 2008; Scott and Lyons, 2012; e.g., Tribouillard et al., 2006).

432 The Fe- and Mn-rich stratigraphic interval in the upper part of the FB₁ Member has
433 been related to a progressive oxidation of Fe(II) and Mn(II) delivered with deep, anoxic
434 waters upwelled across the chemocline towards shallow, oxygenated waters (Fig. 5a; Ossa
435 Ossa *et al.*, 2018). The Fe- and Mn-rich deposits are thought to be derived from precipitation
436 of Fe(III) and Mn(IV) (oxyhydr)oxides in the water column, followed by conversion to
437 carbonate minerals through early diagenetic dissimilatory reduction of these compounds by
438 microorganisms in association with organic matter oxidation. The moderate Mn enrichment in
439 the FB₂ Member, stratigraphically above the Mn ores of the Upper FB₁ Member, likely
440 indicates a similar process where aqueous Mn(II) was continuously supplied by upwelling
441 deep anoxic waters to the depositional site. Consistent with this interpretation, the FB₂
442 Member sediments shows iron enrichment in carbonate minerals with Fe_{carb} fraction
443 contributing up to 41% to the total Fe_{HR} reservoir (Table S2). Since the proportion of
444 Fe_{PRS}/Fe_T in studied samples is much lower than the Phanerozoic average, it is unlikely that
445 iron of the carbonate fraction was post-depositionally transferred to the silicate pool, which
446 supports preservation of the original Fe_{HR}/Fe_T signal. In addition, relatively high Mn content in
447 the FB₂ Member could also reflect deposition near the redox boundary (Calvert and
448 Pedersen, 1993). While the seafloor colonization by mat-building cyanobacteria in the MRS
449 and large sulfur isotope fractionations have been used to infer an oxygenated, shallow-
450 marine depositional environment in the photic zone for the FB₂ Member (Aubineau *et al.*,
451 2018; El Albani *et al.*, 2019; Reynaud *et al.*, 2017), our Fe-speciation data for this interval
452 show evidence for intermittently oxic to anoxic bottom-water conditions likely in proximity to
453 the chemocline (Fig. 5b). Weak to moderate correlations are observed between P and both
454 Ti ($R^2 = 0.17$, $p < 0.08$) and Al ($R^2 = 0.31$, $p < 0.02$) in the studied host sediments (Fig. S3),
455 suggesting that detrital P delivery was not significant, as Ti and Al are usually taken to be
456 detrital tracers (Filippelli *et al.*, 2003; Tribouillard *et al.*, 2006). Moreover, O₂-depleted bottom-
457 waters may limit P burial through reductive dissolution and recycling of primary
458 Fe(III)(oxyhydr)oxides and remineralization of organic matter in sulfate-rich water column and
459 pore-waters (Ingall and Jahnke, 1994). Hence, P input from upwelling waters (Fig. 5b) might
460 be responsible for the minor P enrichment in our black shale samples. Considering the
461 absence of relationship between the sedimentation rate and P and TOC concentrations in
462 modern environments (Ingall and Van Cappellen, 1990), the elevated TOC content in the
463 black shales of the FB₂ Member could reflect high rates of primary organic productivity
464 stimulated by this P input.

465 While the absence of Mo enrichment is consistent with the Fe-speciation data arguing
466 against persistently euxinic conditions, anoxia cannot account for the lack of U and V
467 enrichment because their accumulation is expected under oxygen-deficient depositional

468 conditions (Tribovillard *et al.*, 2006). In addition, the absence of Co, Cu, and Ni enrichment
469 despite appreciable amounts of organic carbon in the black shales is unusual since these
470 elements are usually enriched in sedimentary rocks in association with organic matter as
471 organometallic complexes (Tribovillard *et al.*, 2006). One possible explanation is that the
472 basinal or global inventory of dissolved redox-sensitive trace metals was depleted.
473 Considering that trace metal reservoir size exerts a first-order control on the magnitude of
474 enrichment (Partin *et al.*, 2013; Scott *et al.*, 2008; Tribovillard *et al.*, 2008), limited metal
475 availability could have played an important role in the absence of Co, Cu, and Ni
476 accumulation. Indeed, trace metals are drawn down almost quantitatively even in some
477 modern anoxic marine environments (*e.g.*, the Black Sea; Algeo & Lyons, 2006), and the
478 same process has been invoked to explain limited trace metal enrichment in the roughly
479 coeval *ca.* 2.0 Ga Zaonega Formation (Kipp *et al.*, 2020). In addition to the redox control on
480 trace metal depletion, basin restriction from the global ocean could have also facilitated
481 depletion of the basinal reservoirs of U, V, Co, Cu, and Ni. The tectonic setting of the
482 Francevillian basin could be invoked to explain basinal restriction from the open ocean or at
483 least to limited connection to the global ocean inventory, especially behind the forebulge (*cf.*
484 Bankole *et al.*, 2018; Ossa Ossa *et al.*, 2020). Similarly, the absence of wave-related
485 features or storm beds in the FB₂ Member sandstones may indicate that the depositional
486 setting was sheltered by the fault-bounded compartmentalization of the Francevillian basin
487 (Reynaud *et al.*, 2017). It is thus reasonable to assume that geochemical conditions in the
488 Upper FB Formation reflect basin-scale processes. Furthermore, high sedimentation rate of
489 siliciclastic deposits in the FB₂ Member (Reynaud *et al.*, 2017) may have diluted the
490 elemental enrichments (Algeo and Lyons, 2006). However, MRS indicate periods with slow
491 sedimentation rate in the basin and yet show no significant enrichment in U and V. Along
492 these lines, we envisage that these data might reflect benthic productivity and limited export
493 of organic matter with associated trace elements from the photic zone. In light of these
494 considerations, we interpret the observed trends in major and trace element concentrations
495 to record upwelling, anoxic deep waters enriched in Fe, Mn, and P.

496 **C and N isotopic fidelity**

497 The C and N isotope composition of sedimentary rocks can be affected by three main stages
498 of post-depositional alteration, including early diagenesis, late-stage burial diagenesis, and
499 metamorphism (Ader *et al.*, 2016). Therefore, before evaluating organic $\delta^{13}\text{C}$ and whole-rock
500 $\delta^{15}\text{N}$ signals, we examined whether post-depositional alteration could have overprinted
501 primary signals.

502 While it has been shown that during the transfer of organic matter from water column
503 to surface sediments the $\delta^{15}\text{N}$ signal of primary producers might be altered, settings with high
504 sedimentation and burial rates, short oxygen-exposure time, and high export production tend
505 to faithfully record the isotopic composition of planktonic organisms (Robinson et al., 2012;
506 Tesdal et al., 2013). These characteristics match those inferred for the depositional site of
507 the FB₂ Member, suggesting that the observed N isotope ratios might be reflective of water-
508 column processes; however, a detailed investigation of possible diagenetic effects on C and
509 N isotope ratios is still warranted.

510 One way to gauge diagenetic reworking of sedimentary organic matter is with C:N
511 ratios. Molar C:N values in modern oceanic phytoplankton range from about 4 to 10 (Ader et
512 al., 2016; Gruber and Galloway, 2008), and the preferential oxidation of labile, N-rich
513 components of marine biomass during its sinking through water column and in sediments
514 can increase the C:N ratio in sedimentary rocks. The analyzed MRS and host sediment
515 samples predominantly show C:N values between 5 and 100 (Fig. 6). These values are
516 similar to those from other Precambrian sedimentary successions that experienced moderate
517 post-depositional thermal alteration (*i.e.* below greenschist facies; Koehler *et al.*, 2017; Kipp
518 *et al.*, 2018; Chang *et al.*, 2019), and are consistent with a moderate diagenetic increase in
519 C:N ratios.

520 Anoxic diagenetic conditions during deposition of the FB₂ Member are suggested by
521 the occurrence of Fe- and Mn-bearing carbonate minerals formed by microbial reduction of
522 Fe- and Mn-oxyhydroxides (Ossa Ossa et al., 2018) as well as by the abundance of pyrite
523 with early diagenetic S isotope signature (highly negative $\delta^{34}\text{S}$ values). Both early and late
524 stage diagenesis under anoxic conditions could slightly modify the $\delta^{15}\text{N}_{\text{WR}}$ values (Ader et al.,
525 2016). The first step in this process is the degradation of organic-bound N (*i.e.*,
526 remineralization), which releases N as NH_4^+ to pore-waters below the sediment-water
527 interface. Then, NH_4^+ can be incorporated into the interlayers of illite via substitution for
528 potassium cations (Schroeder and McLain, 1998; Williams et al., 1995; Williams and Ferrell
529 Jr, 1991). The phyllosilicate-bound N phases represent up to half of TN content in modern
530 sediments (Müller, 1977). Our dataset shows a strong positive co-variation ($R^2 = 0.74$, $p < 2$
531 $\times 10^{-9}$) between TN and K (wt.%), supporting NH_4^+ fixation in K-rich clays during the
532 breakdown of organic matter (Fig. S4a). Nonetheless, there is no apparent correlation
533 between $\delta^{15}\text{N}_{\text{WR}}$ and K (wt.%) ($R^2 = 0.11$, $p < 0.12$), which suggests that this diagenetic
534 pathway did not affect the whole-rock $\delta^{15}\text{N}$ signal.

535 Another post-depositional process that elevates C:N ratios and can alter whole-rock C
536 and N isotopic signals is thermal maturation. Specifically, diagenesis and metamorphism can

537 lead to enrichment in heavy C and N isotopes in the remaining reservoir (Bebout & Fogel,
538 1992; Stüeken *et al.*, 2017a), although the $\delta^{15}\text{N}_{\text{WR}}$ composition may not significantly change
539 at metamorphic grades up to lower greenschist facies (Ader *et al.*, 2006, 1998; Boudou *et al.*,
540 2008; Stüeken *et al.*, 2017a). Thermal alteration of organic molecules also drives the
541 depletion of N relative to C (Ader *et al.*, 1998; Bebout and Fogel, 1992). Combined, these
542 processes should result in correlation between $\delta^{13}\text{C}_{\text{org}}$ and TOC as well as $\delta^{13}\text{C}_{\text{org}}$ and C:N_{WR}.
543 With increasing burial depth and metamorphism, thermal alteration of organic matter could
544 shift $\delta^{15}\text{N}_{\text{WR}}$ values up by <1‰ in lower greenschist facies, 1 to 2‰ in greenschist facies, and
545 up to 4‰ in amphibolite facies (Bebout & Fogel, 1992; Stüeken *et al.*, 2017a). The
546 Franceville sub-basin was not affected by metamorphism (Gauthier-Lafaye and Weber,
547 1989; Ngombi-Pemba *et al.*, 2014), suggesting a maximum increase in whole-rock $\delta^{15}\text{N}$
548 values by less than 1‰ due to burial. Typically, strong co-variation among $\delta^{15}\text{N}_{\text{WR}}$ and TN,
549 $\delta^{15}\text{N}_{\text{WR}}$ and C:N, $\delta^{13}\text{C}_{\text{org}}$ and TOC as well as $\delta^{13}\text{C}_{\text{org}}$ and C:N_{WR} are taken to indicate
550 metamorphic alteration, as light isotopes are more mobile than heavier ones and N is more
551 mobile than C (Bebout & Fogel, 1992; Stüeken *et al.*, 2017a). In contrast, these correlations
552 are not observed across our Francevillian Group FB₂ Member MRS and host-sediment
553 samples (Fig. S4b), suggesting that thermal maturation did not substantially alter whole-rock
554 C and N isotope signatures. In addition, the $\delta^{15}\text{N}_{\text{kerogen}}$ values are slightly enriched (on
555 average by +1.6‰) relative to corresponding $\delta^{15}\text{N}_{\text{WR}}$ values in our samples (Table S3), which
556 is in good agreement with the pattern shown by most of the unmetamorphosed rocks studied
557 by Stüeken *et al.* (2017a). The partitioning between kerogen- and mineral-bound nitrogen
558 within the whole rock under progressive metamorphism is marked by the increase of the
559 isotopic offset between kerogen and whole-rock $\delta^{15}\text{N}$ values (Stüeken *et al.*, 2017a; Kipp *et*
560 *al.*, 2018), with kerogen becoming lighter than the whole-rock, which is not observed in our
561 Francevillian Group FB₂ Member samples, consistent with the unmetamorphosed facies.
562 Thus, we take our C and N isotope data as minimally affected by post-depositional isotopic
563 fractionation.

564 **Interpretation of C and N isotope data for the FB₂ Member**

565 Carbon cycling

566 Autotrophic microorganisms preferentially incorporate ^{12}C from CO_2 , CH_4 , or other carbon-
567 bearing organic molecules into their biomass as a function of their carbon fixation pathway,
568 resulting in fractionation of carbon isotopes (Zerkle *et al.*, 2005). Carbon isotope fractionation
569 during primary productivity is also affected by a combination of other factors, including
570 growth rate, dissolved CO_2 level, and the ratio of volume to surface area (Hayes *et al.*, 1999).
571 For the MRS and host sediments, the fractionation of C isotopes from the contemporaneous

572 dissolved inorganic carbon ($\Delta^{13}\text{C}$) was on average 35 to 44‰ (1 σ confidence interval), using
573 the $\delta^{13}\text{C}_{\text{carb}}$ within the black shales of the FB Formation with the average of $6.6 \pm 1.2\%$ (1 σ , n
574 = 10; ranging from 5.5 to 9.6‰; El Albani *et al.*, 2010). The latter $\delta^{13}\text{C}_{\text{carb}}$ values are similar to
575 those of marine carbonates deposited during the LE (Bekker *et al.*, 2008).

576 The $\delta^{13}\text{C}_{\text{org}}$ values of the FB₂ Member host sediments are unlikely to reflect the
577 activity of photoautotrophic fixation alone. Instead, they may be pointing to the contribution of
578 organic matter derived from multiple carbon fixation pathways, assuming that the $^{13}\text{C}/^{12}\text{C}$
579 ratio of atmospheric CO₂ has not changed significantly through time. Indeed, modern
580 photosynthesizers that assimilate dissolved inorganic carbon in equilibrium with atmospheric
581 CO₂ (with a composition of -7‰) fractionate carbon isotopes by up to about 30‰ through the
582 Calvin–Benson–Bassham cycle (Karhu and Bekker, 2020; Schidlowski, 1987; Zerkle *et al.*,
583 2005). The substantially larger fractionations between organic and inorganic carbon as
584 recorded by the black shale samples likely reflect secondary productivity in the water column
585 and near the sediment–water interface (cf. Hayes *et al.*, 1999). Specifically, carbon fixation
586 through the reductive acetyl-coenzyme A (=acetyl-CoA) pathway of strictly anaerobic
587 microorganisms, including autotrophic and acetoclastic methanogens, and some sulfate
588 reducers, induces fractionations as large as 40‰, and thus contributing strongly depleted
589 $^{13}\text{C}_{\text{org}}$ to the sedimentary rock record (Schidlowski, 1987; Zerkle *et al.*, 2005; Stüeken *et al.*,
590 2017b). However, carbon fixation pathways that fractionate biomass by more than about
591 40‰ are unknown (Karhu and Bekker, 2020; Schidlowski, 1987; Zerkle *et al.*, 2005).
592 Accordingly, the incorporation of isotopically “superlight” organic carbon into biomass as
593 observed in some of our samples could only be explained by the involvement of secondary
594 productivity, *e.g.* methanotrophy, believed to have been prominent during the deposition of
595 the FB Member (Gauthier-Lafaye and Weber, 2003).

596 Such microbial activity relies on methane oxidation during which variable electron
597 acceptors are used; both aerobic and anaerobic processes may promote methane oxidation.
598 The large seawater sulfate reservoir at the time of deposition of the Francevillian Group
599 (Bekker *et al.*, 2006; Canfield *et al.*, 2013; Schröder *et al.*, 2008) suggests that the anaerobic
600 oxidation of methane could have occurred with sulfate as an oxidant (*i.e.*, anaerobic
601 oxidation of methane coupled to sulfate reduction). However, we cannot rule out the
602 possibility of aerobic methane oxidation occurring in this setting as well, considering Fe-
603 speciation evidence for intermittently oxic to anoxic bottom-water conditions in the likely
604 proximity of the chemocline. Particularly, Cu is an essential cofactor in the methane
605 monooxygenase, the most active enzyme involved during aerobic biological methane
606 oxidation (Knapp *et al.*, 2007). Given the large amount of land-derived Cu supplied to the
607 oceans during both the GOE and LE (Chi Fru *et al.*, 2016), it is likely that Cu was available to

608 support aerobic methanotrophy at the chemocline (Chi Fru, 2011; Chi Fru et al., 2011).
609 Collectively, highly negative $\delta^{13}\text{C}_{\text{org}}$ values beyond the range of phototroph-derived organic
610 matter in the studied sediments argue for the addition of isotopically light biomass recording
611 biological methane cycling below or at the redoxcline (Fig. 5b).

612 The presence of EST, “fairy ring” structures, tufted morphology, and structures
613 interpreted as gas bubbles related to oxygen production in microbial mats suggest that
614 filamentous cyanobacteria were responsible for the development of the Francevillian Group
615 MRS (Aubineau et al., 2019, 2018). However, carbon isotope fractionation ($>40\text{‰}$) in the
616 MRS also points to methane-based metabolism as explained above (Fig. 5b). In this context,
617 the whole range of $\delta^{13}\text{C}_{\text{org}}$ values in different MRS morphotypes likely reflect the extent to
618 which CO_2 fixation, methane production, and methanotrophy operated in this sedimentary
619 setting.

620 The absence of extensive pyritization in the pyrite-poor MRS, relative to pyritized
621 MRS, is counterintuitive because a large amount of organic matter is still preserved (Tables
622 S2, S3). However, this could be explained by a change in physical and chemical
623 environmental factors at the FB_{2a} - FB_{2b} unit boundary where high-energy conditions and rapid
624 burial in the depositional setting of the pyrite-poor MRS would have limited the extension of
625 sulfidic pore waters (Aubineau et al., 2020). In addition, the mat thickness seems to play a
626 role in the microbial community assemblage (Suarez et al., 2019), although external
627 environmental parameters (*e.g.*, hydrodynamic regime) also influence the microbial
628 architecture (Battin et al., 2003). The mat thickness allows the expression of distinct redox
629 gradients and internal carbon recycling styles whereby thick mats develop a wide anoxic
630 zone (Suarez et al., 2019). This is consistent with our observations that the poorly pyritized
631 MRS are <0.5 cm thick, whereas the thicker pyritized MRS (Aubineau et al., 2020) promoted
632 the development of the anoxic/sulfidic conditions required to enable strong pyritization.
633 Collectively, the high-energy depositional environment and mat thickness might have been
634 the dominant control on pyrite formation in the FB_2 Member MRS.

635 Nitrogen cycling

636 The geochemical data described above indicate the development of intermittently oxic to
637 anoxic bottom-water conditions in likely proximity to the redoxcline during deposition of the
638 FB_2 Member. Well-oxygenated conditions were inferred for the depositional setting of the
639 overlying FC_1 Member (Canfield et al., 2013), in which a pervasive aerobic N cycle has been
640 recognized (Kipp et al., 2018). The latter is characterized by positive $\delta^{15}\text{N}$ values (from $+4\text{‰}$
641 to $+7\text{‰}$) that have been linked to rapid nitrification followed by non-quantitative denitrification

642 in the water column. Such values clearly indicate the predominance of nitrate-using
643 ecosystem that may have comprised both prokaryotes and eukaryotes.

644 In contrast, the N isotope composition of our samples is consistent with the
645 development of an anaerobic N cycle. $\delta^{15}\text{N}$ values between -2‰ and +1‰ usually reflect
646 biological N_2 fixation by cyanobacteria using Mo-bearing nitrogenase (Bauersachs et al.,
647 2009; Carpenter et al., 1997; Minagawa and Wada, 1986; Zhang et al., 2014). At high Fe^{2+}
648 concentrations (>50 nM), fractionations driven by Mo-based diazotrophy can be as large as -
649 4‰ (Zerkle et al., 2008). The very high Fe/Al ratios in the pyritized MRS horizons point to
650 localized Fe-rich water-column conditions during either the mat growth or early diagenesis
651 where DIR and MSR occurred, which may explain their slightly more negative $\delta^{15}\text{N}$ values
652 (down to -3.3‰; Fig. 3). Alternative nitrogenase enzymes, in which Fe or V replace Mo at the
653 active site, generate even more ^{15}N -depleted biomass with $\delta^{15}\text{N}$ values as low as -8‰
654 (Stüeken et al., 2016; Zhang et al., 2014). The invariable N isotope composition of the
655 atmosphere over the last 3 Ga ($\delta^{15}\text{N}_{\text{air}} \approx 0\text{‰}$; Sano & Pillinger, 1990; Marty *et al.*, 2013),
656 together with minimal post-depositional alteration, suggest that the $\delta^{15}\text{N}_{\text{WR}}$ values for the
657 MRS and black shales correspond to the microbial N_2 fixation by Mo-nitrogenase-utilizing
658 cyanobacteria. The N_2 fixation signal recorded by both the MRS and black shales implicates
659 two possible scenarios: the expression of diazotrophy in benthic habitats and in the water
660 column, and/or the contribution of benthically derived biomass (*i.e.* from MRS) to the organic
661 matter content of the black shales (Fig. 5b). The high TOC, TN, and weakly enriched P
662 contents, at least in the pyrite-poor MRS, suggest that productivity was high, which is
663 consistent with nutrient supply with upwelling, anoxic deep-waters, and/or high burial
664 efficiency due to benthic productivity in microbial mats and anoxic water-column conditions.
665 In contrast to other middle Paleoproterozoic depositional settings, including the broadly
666 correlative Zaonega Formation of Karelia, Russia (Kump et al., 2011) and the overlying FC₁
667 Member of the Franceville sub-basin (Kipp et al., 2018), the FB₂ Member records diazotroph-
668 dominated ecosystem in the coastal area of the upwelling zone where deep, anoxic waters
669 delivered nutrients. Notably, evidence for N_2 -fixing cyanobacteria, similar to that producing
670 modern microbial mats (Herbert, 1999; Woebken et al., 2015), points to processes in the
671 Paleoproterozoic Franceville sub-basin that are reminiscent of modern coastal settings in an
672 oxygen-minimum zone.

673 One possibility is that the black shales contain organic matter derived from the
674 microbial mats, such that the mat-derived isotopic signatures of N_2 fixation were imprinted
675 onto the black shale facies. The contribution of microbial mats would result in advanced
676 stages of illitization, induced by a biologically mediated K-enrichment in the living mats
677 (Aubineau et al., 2019); this signature was not observed in the FB_{2b} unit black shales.

678 Furthermore, the petrographically distinct morphological features of microbial mat structures
679 were also not observed in the FB₂ Member black shales (Aubineau et al., 2018).
680 Observations from modern sediments have shown that the contribution of isotopically light
681 biomass from *in situ* microbial growth can decrease sedimentary $\delta^{15}\text{N}$ values by 1 to 2‰
682 during anoxic diagenesis (Lehmann et al., 2002). Such a process could potentially explain
683 the near-zero $\delta^{15}\text{N}$ values in the black shales. However, the petrographic and mineralogical
684 evidence seem to suggest that benthically produced organic matter was not a significant
685 contributor to the studied black shales, which instead potentially implicates two distinct
686 organic matter sources for black shales and microbial mats. Hence, the $\delta^{15}\text{N}_{\text{WR}}$ values of the
687 FB_{2b} unit black shales may reflect the N isotope composition of organic matter delivered from
688 the water column to the sediments. Modern anoxic analogues of a water-column ecosystem
689 dominated by diazotrophs in an otherwise oxygenated and nitrate-replete oceans are known
690 in the Black Sea and Cariaco Basin (Fulton et al., 2012; Thunell et al., 2004). These
691 environments have limited connection to the global ocean, resulting in nitrate depletion. By
692 contrast, the large seawater sulfate reservoir with marine connection in the Francevillian
693 Group FB₂ Member suggests that the depositional environment was not severely restricted
694 with respect to the sulfate reservoir. While it is conceivable that the basin was semi-
695 restricted, leading to depletion of the nitrate reservoir, but not sulfate reservoir due to the
696 high sulfate level at the time of deposition (Bekker et al., 2006; Schröder et al., 2008),
697 allowing negative $\delta^{34}\text{S}$ values in pyrite, as is observed in the Black Sea (Lyons, 1997) – it is
698 also possible that another mechanism contributed to the expression of an anaerobic system
699 dominated by biological N₂ fixation.

700 Nitrogen isotopes along Mesoproterozoic cross-basinal transects have been shown to
701 record aerobic N cycling shoreward, while anaerobic N pathways were restricted to the
702 anoxic deep-water part of the basins (Koehler et al., 2017; Stüeken, 2013). By contrast, the
703 shallow-water depositional setting of the FB₂ Member shows evidence of anaerobic N
704 cycling. Given the high metabolic cost of biological N₂ fixation (16 ATP molecules per
705 molecule of N₂ fixed; Herbert, 1999), the $\delta^{15}\text{N}$ values near 0‰ hint that bioavailable nitrogen
706 was indeed scarce in this environment. Considering that the redox potential of Mn(II)
707 oxidation is higher than that for NH₄⁺ oxidation, nitrifying microbes could have promoted
708 oxidation of NH₄⁺ to NO₂⁻ and NO₃⁻ since the relevant redox threshold was crossed, as
709 indicated by the extensive Mn enrichment in the FB Formation. Our data rather suggest that
710 the buildup of a nitrate reservoir was not strong enough to leave a positive isotopic fingerprint
711 (*i.e.*, isotopically heavy residual NO₃⁻) via non-quantitative denitrification. In the modern
712 ocean, bioavailable P, N, and Fe are the main nutrient controls on biological productivity in
713 coastal upwelling systems (Capone and Hutchins, 2013). Therefore, P or Fe scarcity could

714 have been the main limiting factor in the production of bioavailable nitrogen. Under
715 widespread anoxic conditions as herein inferred to develop at least episodically in the
716 Franceville sub-basin, it has been hypothesized that phosphorus availability would be
717 restricted via adsorption onto Fe minerals (Reinhard et al., 2017) and high organic carbon
718 burial efficiency because of a scarcity of oxidants for organic remineralization (Kipp and
719 Stüeken, 2017), hampering rates of primary productivity. In contrast, the sizeable seawater
720 sulfate reservoir during deposition of the FB₂ Member sediments would not have limited the
721 P regeneration. We also observe high to moderate TOC concentrations and weak P
722 enrichment in sediments, which contrast with expectations for oligotrophic environments. In
723 modern surface waters of upwelling zones, a shortage of iron induces low N₂ fixation rates
724 (Sohm et al., 2011). Petrographic and geochemical data, combined with Fe speciation
725 results, argue against a significant Fe limitation in the basin during deposition of the FB₂
726 Member. Molybdenum, one of the essential constituents of the nitrogenase enzyme (Williams
727 and Fraústo da Silva, 2002), could have been a limiting nutrient for biological activity
728 throughout the mid-Proterozoic (Anbar and Knoll, 2002) as it is scavenged from euxinic
729 seawater that episodically and locally developed in upwelling zones in the oceans along
730 continental margins and in intracratonic basins during the mid-Proterozoic. We cannot
731 completely rule out the possibility of Mo limitation during deposition of the FB₂ Member, since
732 low Mo content has been inferred for the Proterozoic oceans (Reinhard et al., 2013; Scott et
733 al., 2008). However, given that Mo-nitrogenase has been operating at Earth's surface since
734 ~3.2 Ga (Stüeken et al., 2015), when Mo was likely more scarce in the marine environment,
735 it is perhaps unlikely that widespread Mo limitation occurred in the mid-Paleoproterozoic,
736 particularly during the "oxygen overshoot" interval during which marine trace metal
737 inventories are thought to have expanded (Bekker and Holland, 2012; Kipp et al., 2017;
738 Partin et al., 2013; Scott et al., 2008).

739 The threshold at which NH₄⁺ is rapidly oxidized via bacterial nitrification is modeled at
740 low micromolar (>1.8 to 11 μM) dissolved oxygen concentrations (Cheng et al., 2019; Fennel
741 et al., 2005; Kipp et al., 2018). Estimates of absolute atmospheric O₂ level in the
742 Paleoproterozoic remain elusive, however, a massive increase in atmospheric O₂ content
743 has been inferred for the LE (Bekker and Holland, 2012; Karhu and Holland, 1996). It seems
744 likely that atmospheric oxygen was maintained at levels high enough to sustain widespread
745 nitrification in the oceans and a substantial dissolved nitrate reservoir during deposition of the
746 FB₂ Member. Thus, if the observed δ¹⁵N values are indicative of locally developed nitrate
747 limitation, this would likely have been a transient state that ultimately yielded to more
748 oxygenated and nitrate-replete conditions.

749 In this regard, we suggest that the observed nitrate limitation was likely modulated by
750 the basin-scale redox structure in the Franceville sub-basin (Fig. 5). Specifically, the flux of
751 hydrothermally sourced reductants and nutrients may have controlled the redox state at the
752 depositional site for the upper part of the FB₁ Member (Fig. 5a) (Ossa Ossa et al., 2018),
753 involving the upwelling of deep anoxic waters into oxic, shallow-water coastal settings. The
754 large flux of reductants (*e.g.*, Mn and Fe) and nutrients (*e.g.*, P) could have transiently shifted
755 redox conditions to be oxygen-depleted and, thus, triggered denitrification. In modern and
756 ancient coastal upwelling systems with strong inputs of P, intense denitrification and
757 anammox result in a rapid N removal in oxygen-minimum zones, which in turn triggers the
758 surface activity of N₂-fixing photoautotrophs (Capone et al., 1998; Deutsch et al., 2007; Wang
759 et al., 2018). Due to the scarcity of NO₃⁻ relative to PO₄³⁻, the N:P ratio of the water column in
760 these settings reaches below the Redfield ratio of 16:1 in phytoplankton biomass (Redfield,
761 1958). The nitrate limitation in surface waters along upwelling transects appears as a natural
762 consequence of high primary productivity. Furthermore, the loss of fixed nitrogen from the
763 ocean has been proposed as a signature of the oxic-anoxic transition (Fennel et al., 2005).
764 This has also been highlighted in the Ediacaran-Phanerozoic settings whereby enhanced
765 denitrification/anammox and sometimes phosphate addition, together with eustatic
766 fluctuations, would have allowed for the expression of N₂ fixation in shallow depositional
767 environments (Chang et al., 2019; Cremonese et al., 2014; Wang et al., 2013). Further, the
768 nitrate reservoir may be severely depleted if the chemocline was relatively shallow,
769 particularly within the photic zone (Ader et al., 2014; Kipp et al., 2018). Accordingly,
770 introduction of deep anoxic waters developed a redoxcline in the Franceville sub-basin
771 during deposition of the upper part of the FB₁ Member (Fig. 5a). Although the overlying water
772 column should have been more oxygenated with sea-level fall leading to deposition of the
773 FB₂ Member, nitrate limitation developed in surface waters due to enhanced flux of nutrients
774 (*e.g.*, P) with upwelling of anoxic deep-waters in a pattern similar to modern oxygen-
775 minimum zones along continental margins (Fig. 5b) and restricted basins. These conditions
776 ultimately led to the drawdown of the reservoir of bioavailable nitrogen due to high rates of
777 denitrification and anammox activity. The lack of evidence for Mo and P biolimitation,
778 combined with N isotope data indicative of an aerobic N cycle during deposition of the
779 overlying FC₁ Member (Kipp et al., 2018), argue for a local, short-lived N scarcity (Figs. 5b,
780 c).

781 **Implications for primary productivity in the Franceville sub-basin**

782 Our results provide evidence for N₂ fixation both in the MRS and water column in the
783 Franceville sub-basin during deposition of the FB₂ Member. N₂ fixation is commonly
784 observed in microbial mats, however, benthic communities should not significantly contribute

785 to the N budget of the overlying water column (Bebout et al., 1994; Herbert, 1999). Rather,
786 cyanobacterial blooms in the water column strive to replenish the bioavailable N pool (Tyrrell,
787 1999). The pervasive episodic input of phosphate during deposition of the FB₂ Member
788 suggests that N₂ fixation sustained primary productivity during deposition of the FB₂ Member.
789 Modelling indicates that a high phosphate flux would increase N₂ fixation and bioavailable
790 nitrogen, which in turn invigorates oxygen production and accumulation (Fennel et al., 2005).
791 Although aerobic N cycling during the GOE may have been pervasive as previously
792 suggested (Kipp et al., 2018), our data suggest that regional redox fluctuations – perhaps
793 related to the degree of basinal restriction from the open ocean – controlled the N dynamics
794 in the Franceville sub-basin, which provides insight into heterogeneity of the marine N cycle
795 in the wake of the LE.

796 **Conclusion**

797 The combined study of bottom-water redox proxies and C and N isotopes in the Francevillian
798 Group FB₂ Member MRS and host sediments allowed us to better constrain local redox
799 conditions and microbial biogeochemical cycling at the end of the Lomagundi Event. Our
800 results, summarized in Figure 5, suggest a local, short-lived nitrate scarcity in the water
801 column as well as N₂ fixation by benthic and water-column microbial communities.
802 Importantly, the expression of multiple metabolic C pathways and N₂ fixation in this middle
803 Paleoproterozoic coastal setting points to the existence of biogeochemical C and N cycling in
804 patterns similar to an oxygen-minimum zone developed in a modern coastal upwelling
805 system.

806 Anoxic deep waters were likely upwelled into oxic, shallow coastal settings across the
807 redoxcline during deposition of the upper part of the FB₁ Member (Fig. 5a). The subsequent
808 sea-level fall and a decrease in a flux of reductants, combined with a continued supply of
809 nutrients, led to increased primary productivity and nitrate limitation in the water column as
810 recorded by the FB₂ Member (Fig. 5b). In the face of this nitrate limitation, diazotrophs
811 sustained primary productivity in surface waters, replenishing the bioavailable N pool (Figs.
812 5b, c). These redox conditions were superseded by a return to local oxic water-column
813 conditions that allowed the expansion of nitrate-assimilating organisms during deposition of
814 the overlying FC₁ Member. The transient interval dominated by N₂ fixation was thus
815 controlled by the basinal redox structure and flux of reductants, and, to some extent, by the
816 degree of isolation from the global ocean. Although globally oxic conditions prevailed at this
817 time, our results show that regional redox fluctuations led to local nitrate limitation during the
818 LE. Future work should further elucidate the relationship between these local redox
819 conditions, microbial N₂ fixation, and proliferation of the earliest motile macroorganisms.

820 **Acknowledgments**

821 We acknowledge the support of the Gabonese Government, CENAREST, General Direction
822 of Mines and Geology, and Agence Nationale des Parcs Nationaux of Gabon. This work was
823 supported by La Région Nouvelle Aquitaine, the University of Poitiers, Théodore Monod
824 Doctoral School, and the French Embassy in Libreville, Gabon. We are grateful to Prof. P.
825 Mouguiama Daouda, J.C. Balloche, L. White, and R. Oslisly for their support during field
826 trips. For assistance, we acknowledge C. Laforest, C. Lebailly, Y. Lin, L. Magad-Weiss, A.
827 Meunier, A. Oldroyd, P. Recourt, C. Reedman, and X. Tang. J.A. is particularly thankful to T.
828 Lyons for scientific discussions.

829

830 **References**

- 831 Ader, M., Boudou, J.-P., Javoy, M., Goffé, B., Daniels, E., 1998. Isotope study on organic
832 nitrogen of Westphalian anthracites from the Western Middle field of Pennsylvania (U.S.A.)
833 and from the Bramsche Massif (Germany). *Organic Geochemistry* 29, 315–323.
834 [https://doi.org/10.1016/S0146-6380\(98\)00072-2](https://doi.org/10.1016/S0146-6380(98)00072-2)
- 835 Ader, M., Cartigny, P., Boudou, J.-P., Oh, J.-H., Petit, E., Javoy, M., 2006. Nitrogen isotopic
836 evolution of carbonaceous matter during metamorphism: Methodology and preliminary
837 results. *Chemical Geology* 232, 152–169. <https://doi.org/10.1016/j.chemgeo.2006.02.019>
- 838 Ader, M., Sansjofre, P., Halverson, G.P., Busigny, V., Trindade, R.I.F., Kunzmann, M.,
839 Nogueira, A.C.R., 2014. Ocean redox structure across the Late Neoproterozoic Oxygenation
840 Event: A nitrogen isotope perspective. *Earth and Planetary Science Letters* 396, 1–13.
841 <https://doi.org/10.1016/j.epsl.2014.03.042>
- 842 Ader, M., Thomazo, C., Sansjofre, P., Busigny, V., Papineau, D., Laffont, R., Cartigny, P.,
843 Halverson, G.P., 2016. Interpretation of the nitrogen isotopic composition of Precambrian
844 sedimentary rocks: Assumptions and perspectives. *Chemical Geology* 429, 93–110.
845 <https://doi.org/10.1016/j.chemgeo.2016.02.010>
- 846 Algeo, T.J., Lyons, T.W., 2006. Mo-total organic carbon covariation in modern anoxic marine
847 environments: Implications for analysis of paleoredox and paleohydrographic conditions.
848 *Paleoceanography* 21, PA1016. <https://doi.org/10.1029/2004PA001112>
- 849 Anbar, A.D., Knoll, A.H., 2002. Proterozoic ocean chemistry and evolution: A bioinorganic
850 bridge? *Science* 297, 1137–1142.
- 851 Aubineau, J., El Albani, A., Bekker, A., Chi Fru, E., Somogyi, A., Medjoubi, K., Riboulleau,
852 A., Meunier, A., Konhauser, K.O., 2020. Trace element perspective into the *ca.* 2.1-billion-
853 year-old shallow-marine microbial mats from the Francevillian Group, Gabon. *Chemical*
854 *Geology* 543, 119620. <https://doi.org/10.1016/j.chemgeo.2020.119620>
- 855 Aubineau, J., El Albani, A., Bekker, A., Somogyi, A., Bankole, O.M., Macchiarelli, R.,
856 Meunier, A., Riboulleau, A., Reynaud, J.-Y., Konhauser, K.O., 2019. Microbially induced
857 potassium enrichment in Paleoproterozoic shales and implications for reverse weathering on
858 early Earth. *Nat Commun* 10, 2670. <https://doi.org/10.1038/s41467-019-10620-3>
- 859 Aubineau, J., El Albani, A., Chi Fru, E., Gingras, M., Batonneau, Y., Buatois, L.A., Geffroy,
860 C., Labanowski, J., Laforest, C., Lemée, L., Mángano, M.G., Meunier, A., Pierson-
861 Wickmann, A.-C., Recourt, P., Riboulleau, A., Trentesaux, A., Konhauser, K.O., 2018.
862 Unusual microbial mat-related structural diversity 2.1 billion years ago and implications for
863 the Francevillian biota. *Geobiology* 16, 476–497. <https://doi.org/10.1111/gbi.12296>
- 864 Azziley Azzibrouck, G., 1986. Sédimentologie et géochimie du Francevillien B
865 (protérozoïque inférieur). Métallogénie des gisements de manganèse de Moanda, Gabon.
866 Université Louis Pasteur, Strasbourg.
- 867 Bankole, O.M., El Albani, A., Meunier, A., Gauthier-Lafaye, F., 2015. Textural and paleo-
868 fluid flow control on diagenesis in the Paleoproterozoic Franceville Basin, South Eastern,
869 Gabon. *Precambrian Research* 268, 115–134. <https://doi.org/10.1016/j.precamres.2015.07.008>

870 Bankole, O.M., El Albani, A., Meunier, A., Pambo, F., Paquette, J.-L., Bekker, A., 2018.
871 Earth's oldest preserved K-bentonites in the ca. 2.1 Ga Francevillian Basin, Gabon. *American*
872 *Journal of Science* 318, 409–434. <https://doi.org/10.2475/04.2018.02>

873 Bankole, O.M., El Albani, A., Meunier, A., Rouxel, O.J., Gauthier-Lafaye, F., Bekker, A.,
874 2016. Origin of red beds in the Paleoproterozoic Franceville Basin, Gabon, and implications
875 for sandstone-hosted uranium mineralization. *American Journal of Science* 316, 839–872.

876 Battin, T.J., Kaplan, L.A., Newbold, J.D., Cheng, X., Hansen, C., 2003. Effects of current
877 velocity on the nascent architecture of stream microbial biofilms. *Applied and Environmental*
878 *Microbiology* 69, 5443–5452. <https://doi.org/10.1128/AEM.69.9.5443-5452.2003>

879 Bauersachs, T., Schouten, S., Compaoré, J., Wollenzien, U., Stal, L.J., Sinninghe Damsteé,
880 J.S., 2009. Nitrogen isotopic fractionation associated with growth on dinitrogen gas and
881 nitrate by cyanobacteria. *Limnol. Oceanogr.* 54, 1403–1411.
882 <https://doi.org/10.4319/lo.2009.54.4.1403>

883 Bebout, B.M., Paerl, H.W., Bauer, J.E., Canfield, D.E., Des Marais, D.J., 1994. Nitrogen
884 cycling in microbial mat communities: The quantitative importance of N-fixation and other
885 sources of N for primary productivity, in: Stal, L.J., Caumette, P. (Eds.), *Microbial Mats*
886 *Structure, Development and Environmental Significance*. Springer, Berlin, Heidelberg, pp.
887 265–271.

888 Bebout, G.E., Fogel, M.L., 1992. Nitrogen-isotope compositions of metasedimentary rocks in
889 the Catalina Schist, California: Implications for metamorphic devolatilization history.
890 *Geochimica et Cosmochimica Acta* 56, 2839–2849. [https://doi.org/10.1016/0016-](https://doi.org/10.1016/0016-7037(92)90363-N)
891 [7037\(92\)90363-N](https://doi.org/10.1016/0016-7037(92)90363-N)

892 Bekker, A., El Albani, A., Hofmann, A., Karhu, J.A., Kump, L.R., Ossa Ossa, F., Planavsky,
893 N.J., 2021. The Paleoproterozoic Francevillian succession of Gabon and the Lomagundi-Jatuli
894 event: comment. *Géology*, in press.

895 Bekker, A., Holland, H.D., 2012. Oxygen overshoot and recovery during the early
896 Paleoproterozoic. *Earth and Planetary Science Letters* 317–318, 295–304.
897 <https://doi.org/10.1016/j.epsl.2011.12.012>

898 Bekker, A., Holmden, C., Beukes, N.J., Kenig, F., Eglinton, B., Patterson, W.P., 2008.
899 Fractionation between inorganic and organic carbon during the Lomagundi (2.22–2.1 Ga)
900 carbon isotope excursion. *Earth and Planetary Science Letters* 271, 278–291.
901 <https://doi.org/10.1016/j.epsl.2008.04.021>

902 Bekker, A., Karhu, J.A., Kaufman, A.J., 2006. Carbon isotope record for the onset of the
903 Lomagundi carbon isotope excursion in the Great Lakes area, North America. *Precambrian*
904 *Research* 148, 145–180. <https://doi.org/10.1016/j.precamres.2006.03.008>

905 Bertrand-Sarfati, J., Potin, B., 1994. Microfossiliferous cherty stromatolites in the 2000 Ma
906 Franceville group, Gabon. *Precambrian research* 65, 341–356.

907 Bjerrum, C.J., Canfield, D.E., 2004. New insights into the burial history of organic carbon on
908 the early Earth. *Geochem. Geophys. Geosyst.* 5, Q08001.
909 <https://doi.org/10.1029/2004GC000713>

- 910 Boudou, J.-P., Schimmelmann, A., Ader, M., Mastalerz, M., Sebilou, M., Gengembre, L.,
911 2008. Organic nitrogen chemistry during low-grade metamorphism. *Geochimica et*
912 *Cosmochimica Acta* 72, 1199–1221. <https://doi.org/10.1016/j.gca.2007.12.004>
- 913 Bouton, P., Thiéblemont, D., Gouin, J., Cocherie, A., Guerrot, C., Tegye, M., Pr at, A.,
914 Simo Ndounze, S., Kassadou, A.B., Boulingui, B., Ekhogha, H., Moussavou, M., 2009a.
915 Notice explicative de la Carte g ologique de la R publique du Gabon   1/200,000, feuille
916 Franceville-Boumango, Libreville.
- 917 Bouton, P., Thi blemont, D., Simo Ndounze, S., Goujou, J.C., Kassadou, A.B., Walembe, A.,
918 Boulingui, B., Ekhogha, H., Moussavou, M., Lambert, A., Roberts, D., Deschamps, Y., Pr at,
919 A., 2009b. Carte g ologique de la R publique du Gabon   1/200 000, feuille Franceville -
920 Boumango.
- 921 Bros, R., Stille, P., Gauthier-Lafaye, F., Weber, F., Clauer, N., 1992. Sm-Nd isotopic dating
922 of Proterozoic clay material: An example from the Francevillian sedimentary series, Gabon.
923 *Earth and Planetary Science Letters* 113, 207–218.
- 924 Calvert, S.E., Pedersen, T.F., 1993. Geochemistry of Recent oxic and anoxic marine
925 sediments: Implications for the geological record. *Marine Geology* 113, 67–88.
926 [https://doi.org/10.1016/0025-3227\(93\)90150-T](https://doi.org/10.1016/0025-3227(93)90150-T)
- 927 Canfield, D.E., Glazer, A.N., Falkowski, P.G., 2010. The evolution and future of Earth’s
928 nitrogen cycle. *Science* 330, 192–196. <https://doi.org/10.1126/science.1186120>
- 929 Canfield, D.E., Ngombi-Pemba, L., Hammarlund, E.U., Bengtson, S., Chaussidon, M.,
930 Gauthier-Lafaye, F., Meunier, A., Riboulleau, A., Rollion-Bard, C., Rouxel, O., Asael, D.,
931 Pierson-Wickmann, A.-C., El Albani, A., 2013. Oxygen dynamics in the aftermath of the
932 Great Oxidation of Earth’s atmosphere. *Proceedings of the National Academy of Sciences*
933 110, 16736–16741. <https://doi.org/10.1073/pnas.1315570110>
- 934 Canfield, D.E., Raiswell, R., Westrich, J.T., Reaves, C.M., Berner, R.A., 1986. The use of
935 chromium reduction in the analysis of reduced inorganic sulfur in sediments and shales.
936 *Chemical Geology* 54, 149–155. [https://doi.org/10.1016/0009-2541\(86\)90078-1](https://doi.org/10.1016/0009-2541(86)90078-1)
- 937 Capone, D.G., Hutchins, D.A., 2013. Microbial biogeochemistry of coastal upwelling regimes
938 in a changing ocean. *Nature Geosci* 6, 711–717. <https://doi.org/10.1038/ngeo1916>
- 939 Capone, D.G., Subramaniam, A., Montoya, J.P., Voss, M., Humborg, C., Johansen, A.M.,
940 Siefert, R.L., Carpenter, E.J., 1998. An extensive bloom of the N₂-fixing cyanobacterium
941 *Trichodesmium erythraeum* in the central Arabian Sea. *Marine Ecology Progress Series* 172,
942 281–292.
- 943 Carignan, J., Hild, P., Mevelle, G., Morel, J., Yeghicheyan, D., 2001. Routine analyses of
944 trace elements in geological samples using flow injection and low pressure on-line liquid
945 chromatography coupled to ICP-MS: a study of geochemical reference materials BR, DR-N,
946 UB-N, AN-G and GH. *Geostandards Newsletter* 25, 187–198. <https://doi.org/10.1111/j.1751-908X.2001.tb00595.x>
- 948 Carpenter, E.J., Harvey, H.R., Fry, B., Capone, D.G., 1997. Biogeochemical tracers of the
949 marine cyanobacterium *Trichodesmium*. *Deep Sea Research Part I: Oceanographic Research*
950 *Papers* 44, 27–38. [https://doi.org/10.1016/S0967-0637\(96\)00091-X](https://doi.org/10.1016/S0967-0637(96)00091-X)

- 951 Chang, C., Hu, W., Wang, X., Huang, K.-J., Yang, A., Zhang, X., 2019. Nitrogen isotope
952 evidence for an oligotrophic shallow ocean during the Cambrian Stage 4. *Geochimica et*
953 *Cosmochimica Acta* 257, 49–67. <https://doi.org/10.1016/j.gca.2019.04.021>
- 954 Cheng, C., Busigny, V., Ader, M., Thomazo, C., Chaduteau, C., Philippot, P., 2019. Nitrogen
955 isotope evidence for stepwise oxygenation of the ocean during the Great Oxidation Event.
956 *Geochimica et Cosmochimica Acta* 261, 224–247. <https://doi.org/10.1016/j.gca.2019.07.011>
- 957 Chi Fru, E., 2011. Copper biogeochemistry: A cornerstone in aerobic methanotrophic
958 bacterial ecology and activity? *Geomicrobiology Journal* 28, 601–614.
959 <https://doi.org/10.1080/01490451.2011.581325>
- 960 Chi Fru, E., Gray, N.D., McCann, C., Baptista, J. de C., Christgen, B., Talbot, H.M., El
961 Ghazouani, A., Dennison, C., Graham, D.W., 2011. Effects of copper mineralogy and
962 methanobactin on cell growth and sMMO activity in *Methylosinus trichosporium* OB3b.
963 *Biogeosciences* 8, 2887–2894. <https://doi.org/10.5194/bg-8-2887-2011>
- 964 Chi Fru, E., Kiliyas, S., Ivarsson, M., Rattray, J.E., Gkika, K., McDonald, I., He, Q., Broman,
965 C., 2018. Sedimentary mechanisms of a modern banded iron formation on Milos Island,
966 Greece. *Solid Earth* 9, 573–598. <https://doi.org/10.5194/se-9-573-2018>
- 967 Chi Fru, E., Rodríguez, N.P., Partin, C.A., Lalonde, S.V., Andersson, P., Weiss, D.J., El
968 Albani, A., Rodushkin, I., Konhauser, K.O., 2016. Cu isotopes in marine black shales record
969 the Great Oxidation Event. *Proc Natl Acad Sci USA* 113, 4941–4946.
970 <https://doi.org/10.1073/pnas.1523544113>
- 971 Chi Fru, E., Somogyi, A., El Albani, A., Medjoubi, K., Aubineau, J., Robbins, L.J., Lalonde,
972 S.V., Konhauser, K.O., 2019. The rise of oxygen-driven arsenic cycling at *ca.* 2.48 Ga.
973 *Geology* 47, 243–246. <https://doi.org/10.1130/G45676.1>
- 974 Clarkson, M.O., Poulton, S.W., Guilbaud, R., Wood, R.A., 2014. Assessing the utility of
975 Fe/Al and Fe-speciation to record water column redox conditions in carbonate-rich sediments.
976 *Chemical Geology* 382, 111–122. <https://doi.org/10.1016/j.chemgeo.2014.05.031>
- 977 Cremonese, L., Shields-Zhou, G.A., Struck, U., Ling, H.-F., Och, L.M., 2014. Nitrogen and
978 organic carbon isotope stratigraphy of the Yangtze Platform during the Ediacaran–Cambrian
979 transition in South China. *Palaeogeography, Palaeoclimatology, Palaeoecology* 398, 165–186.
980 <https://doi.org/10.1016/j.palaeo.2013.12.016>
- 981 Dalsgaard, T., Thamdrup, B., Canfield, D.E., 2005. Anaerobic ammonium oxidation
982 (anammox) in the marine environment. *Research in Microbiology* 156, 457–464.
983 <https://doi.org/10.1016/j.resmic.2005.01.011>
- 984 Dennen, K.O., Johnson, C.A., Otter, M.L., Silva, S.R., Wandless, G.A., 2006. $\delta^{15}\text{N}$ and non-
985 carbonate $\delta^{13}\text{C}$ values for two petroleum source rock reference materials and a marine
986 sediment reference material. U. S. Geological Survey Open File Report 2006–1071.
- 987 Deutsch, C., Sarmiento, J.L., Sigman, D.M., Gruber, N., Dunne, J.P., 2007. Spatial coupling
988 of nitrogen inputs and losses in the ocean. *Nature* 445, 163–167.
989 <https://doi.org/10.1038/nature05392>
- 990 El Albani, A., Bengtson, S., Canfield, D.E., Bekker, A., Macchiarelli, R., Mazurier, A.,

- 991 Hammarlund, E.U., Boulvais, P., Dupuy, J.-J., Fontaine, C., Fürsich, F.T., Gauthier-Lafaye,
 992 F., Janvier, P., Javaux, E., Ossa, F.O., Pierson-Wickmann, A.-C., Riboulleau, A., Sardini, P.,
 993 Vachard, D., Whitehouse, M., Meunier, A., 2010. Large colonial organisms with coordinated
 994 growth in oxygenated environments 2.1 Gyr ago. *Nature* 466, 100–104.
 995 <https://doi.org/10.1038/nature09166>
- 996 El Albani, A., Bengtson, S., Canfield, D.E., Riboulleau, A., Rollion Bard, C., Macchiarelli,
 997 R., Ngombi Pemba, L., Hammarlund, E., Meunier, A., Moubiya Mouele, I., Benzerara, K.,
 998 Bernard, S., Boulvais, P., Chaussidon, M., Cesari, C., Fontaine, C., Chi-Fru, E., Garcia Ruiz,
 999 J.M., Gauthier-Lafaye, F., Mazurier, A., Pierson-Wickmann, A.C., Rouxel, O., Trentesaux,
 1000 A., Vecoli, M., Versteegh, G.J.M., White, L., Whitehouse, M., Bekker, A., 2014. The 2.1 Ga
 1001 old Francevillian biota: Biogenicity, taphonomy and biodiversity. *PLoS ONE* 9, e99438.
 1002 <https://doi.org/10.1371/journal.pone.0099438>
- 1003 El Albani, A., Mangano, M.G., Buatois, L.A., Bengtson, S., Riboulleau, A., Bekker, A.,
 1004 Konhauser, K., Lyons, T., Rollion-Bard, C., Bankole, O., Lekele Baghekema, S.G., Meunier,
 1005 A., Trentesaux, A., Mazurier, A., Aubineau, J., Lafort, C., Fontaine, C., Recourt, P., Chi
 1006 Fru, E., Macchiarelli, R., Reynaud, J.Y., Gauthier-Lafaye, F., Canfield, D.E., 2019. Organism
 1007 motility in an oxygenated shallow-marine environment 2.1 billion years ago. *Proceedings of*
 1008 *the National Academy of Sciences* 116, 3431–3436. <https://doi.org/10.1073/pnas.1815721116>
- 1009 Farquhar, J., Savarino, J., Airieau, S., Thiemens, M.H., 2001. Observation of wavelength-
 1010 sensitive mass-independent sulfur isotope effects during SO₂ photolysis: Implications for the
 1011 early atmosphere. *Journal of Geophysical Research* 106, 32829–32839.
 1012 <https://doi.org/10.1029/2000JE001437>
- 1013 Fennel, K., Follows, M., Falkowski, P.G., 2005. The co-evolution of the nitrogen, carbon and
 1014 oxygen cycles in the Proterozoic ocean. *American Journal of Science* 305, 526–545.
 1015 <https://doi.org/10.2475/ajs.305.6-8.526>
- 1016 Filippelli, G.M., Latimer, J.C., Murray, R.W., Flores, J.-A., 2007. Productivity records from
 1017 the Southern Ocean and the equatorial Pacific Ocean: Testing the glacial Shelf-Nutrient
 1018 Hypothesis. *Deep Sea Research Part II: Topical Studies in Oceanography* 54, 2443–2452.
 1019 <https://doi.org/10.1016/j.dsr2.2007.07.021>
- 1020 Filippelli, G.M., Sierro, F.J., Flores, J.A., Vázquez, A., Utrilla, R., Pérez-Folgado, M.,
 1021 Latimer, J.C., 2003. A sediment–nutrient–oxygen feedback responsible for productivity
 1022 variations in Late Miocene sapropel sequences of the western Mediterranean.
 1023 *Palaeogeography, Palaeoclimatology, Palaeoecology* 190, 335–348.
 1024 [https://doi.org/10.1016/S0031-0182\(02\)00613-2](https://doi.org/10.1016/S0031-0182(02)00613-2)
- 1025 Fry, B., Jannasch, H.W., Molyneaux, S.J., Wirsén, C.O., Muramoto, J.A., King, S., 1991.
 1026 Stable isotope studies of the carbon, nitrogen and sulfur cycles in the Black Sea and the
 1027 Cariaco Trench. *Deep Sea Research Part A. Oceanographic Research Papers* 38, S1003–
 1028 S1019. [https://doi.org/10.1016/S0198-0149\(10\)80021-4](https://doi.org/10.1016/S0198-0149(10)80021-4)
- 1029 Fulton, J.M., Arthur, M.A., Freeman, K.H., 2012. Black Sea nitrogen cycling and the
 1030 preservation of phytoplankton $\delta^{15}\text{N}$ signals during the Holocene. *Global Biogeochem. Cycles*
 1031 26, GB2030. <https://doi.org/10.1029/2011GB004196>
- 1032 Gauthier-Lafaye, F., Weber, F., 2003. Natural nuclear fission reactors: Time constraints for

- 1033 occurrence, and their relation to uranium and manganese deposits and to the evolution of the
1034 atmosphere. *Precambrian Research* 120, 81–100.
- 1035 Gauthier-Lafaye, F., Weber, F., 1989. The Francevillian (Lower Proterozoic) uranium ore
1036 deposits of Gabon. *Economic Geology* 84, 2267–2285.
- 1037 Gilleaudeau, G.J., Kah, L.C., 2015. Heterogeneous redox conditions and a shallow
1038 chemocline in the Mesoproterozoic ocean: Evidence from carbon–sulfur–iron relationships.
1039 *Precambrian Research* 257, 94–108. <https://doi.org/10.1016/j.precamres.2014.11.030>
- 1040 Gruber, N., Galloway, J.N., 2008. An Earth-system perspective of the global nitrogen cycle.
1041 *Nature* 451, 293–296. <https://doi.org/10.1038/nature06592>
- 1042 Gumsley, A.P., Chamberlain, K.R., Bleeker, W., Söderlund, U., De Kock, M.O., Larsson,
1043 E.R., Bekker, A., 2017. Timing and tempo of the Great Oxidation Event. *Proceedings of the*
1044 *National Academy of Sciences* 114, 1811–1816. <https://doi.org/10.1073/pnas.1608824114>
- 1045 Hannah, J.L., Stein, H.J., Zimmerman, A., Yang, G., Melezhik, V.A., Filippov, M.M.,
1046 Turgeon, S.C., Creaser, R.A., 2008. Re-Os geochronology of a 2.05 Ga fossil oil field near
1047 Shunga, Karelia, NW Russia. Presented at the The 33rd International Geological Congress,
1048 Oslo.
- 1049 Hayes, J.M., Strauss, H., Kaufman, A.J., 1999. The abundance of ^{13}C in marine organic
1050 matter and isotopic fractionation in the global biogeochemical cycle of carbon during the past
1051 800 Ma. *Chemical Geology* 161, 103–125. [https://doi.org/10.1016/S0009-2541\(99\)00083-2](https://doi.org/10.1016/S0009-2541(99)00083-2)
- 1052 Herbert, R.A., 1999. Nitrogen cycling in coastal marine ecosystems. *FEMS Microbiol Rev*
1053 23, 563–590. <https://doi.org/10.1111/j.1574-6976.1999.tb00414.x>
- 1054 Holland, H.D., 2002. Volcanic gases, black smokers, and the Great Oxidation Event.
1055 *Geochimica et Cosmochimica Acta* 66, 3811–3826.
- 1056 Horie, K., Hidaka, H., Gauthier-Lafaye, F., 2005. U-Pb geochronology and geochemistry of
1057 zircon from the Franceville series at Bidoudouma, Gabon. Presented at the 15th Annual
1058 Goldschmidt Conference, Moscow, United States.
- 1059 Hotinski, R.M., Kump, L.R., Arthur, M.A., 2004. The effectiveness of the Paleoproterozoic
1060 biological pump: A $\delta^{13}\text{C}$ gradient from platform carbonates of the Pethei Group (Great Slave
1061 Lake Supergroup, NWT). *GSA Bulletin* 116, 539–554. <https://doi.org/10.1130/B25272.1>
- 1062 Ingall, E., Jahnke, R., 1994. Evidence for enhanced phosphorus regeneration from marine
1063 sediments overlain by oxygen depleted waters. *Geochimica et Cosmochimica Acta* 58, 2571–
1064 2575. [https://doi.org/10.1016/0016-7037\(94\)90033-7](https://doi.org/10.1016/0016-7037(94)90033-7)
- 1065 Ingall, E.D., Van Cappellen, P., 1990. Relation between sedimentation rate and burial of
1066 organic phosphorus and organic carbon in marine sediments. *Geochimica et Cosmochimica*
1067 *Acta* 54, 373–386. [https://doi.org/10.1016/0016-7037\(90\)90326-G](https://doi.org/10.1016/0016-7037(90)90326-G)
- 1068 Kah, L.C., Lyons, T.W., Chesley, J.T., 2001. Geochemistry of a 1.2 Ga carbonate-evaporite
1069 succession, northern Baffin and Bylot Islands: implications for Mesoproterozoic marine
1070 evolution. *Precambrian Research* 111, 203–234. [https://doi.org/10.1016/S0301-](https://doi.org/10.1016/S0301-9268(01)00161-9)
1071 [9268\(01\)00161-9](https://doi.org/10.1016/S0301-9268(01)00161-9)

- 1072 Karhu, J.A., Bekker, A., 2020. Carbon Isotopes in the Solar System, in: Gargaud, M., Irvine,
1073 W.M., Amils, R., Cleaves, H.J., Pinti, D., Cernicharo Quintanilla, J., Viso, M. (Eds.),
1074 Encyclopedia of Astrobiology. Springer, Berlin, Heidelberg. [https://doi.org/10.1007/978-3-](https://doi.org/10.1007/978-3-642-27833-4_5395-1)
1075 [642-27833-4_5395-1](https://doi.org/10.1007/978-3-642-27833-4_5395-1)
- 1076 Karhu, J.A., Holland, H.D., 1996. Carbon isotopes and the rise of atmospheric oxygen.
1077 *Geology* 24, 867–870. [https://doi.org/10.1130/0091-](https://doi.org/10.1130/0091-7613(1996)024<0867:CIATRO>2.3.CO;2)
1078 [7613\(1996\)024<0867:CIATRO>2.3.CO;2](https://doi.org/10.1130/0091-7613(1996)024<0867:CIATRO>2.3.CO;2)
- 1079 Kipp, M.A., Lepland, A., Buick, R., 2020. Redox fluctuations, trace metal enrichment and
1080 phosphogenesis in the ~2.0 Ga Zaonega Formation. *Precambrian Research* 343, 105716.
1081 <https://doi.org/10.1016/j.precamres.2020.105716>
- 1082 Kipp, M.A., Stüeken, E.E., 2017. Biomass recycling and Earth’s early phosphorus cycle. *Sci.*
1083 *Adv.* 3, eaao4795. <https://doi.org/10.1126/sciadv.aao4795>
- 1084 Kipp, M.A., Stüeken, E.E., Bekker, A., Buick, R., 2017. Selenium isotopes record extensive
1085 marine suboxia during the Great Oxidation Event. *Proc Natl Acad Sci USA* 114, 875–880.
1086 <https://doi.org/10.1073/pnas.1615867114>
- 1087 Kipp, M.A., Stüeken, E.E., Yun, M., Bekker, A., Buick, R., 2018. Pervasive aerobic nitrogen
1088 cycling in the surface ocean across the Paleoproterozoic Era. *Earth and Planetary Science*
1089 *Letters* 500, 117–126. <https://doi.org/10.1016/j.epsl.2018.08.007>
- 1090 Knapp, C.W., Fowle, D.A., Kulczycki, E., Roberts, J.A., Graham, D.W., 2007. Methane
1091 monooxygenase gene expression mediated by methanobactin in the presence of mineral
1092 copper sources. *Proceedings of the National Academy of Sciences* 104, 12040–12045.
1093 <https://doi.org/10.1073/pnas.0702879104>
- 1094 Koehler, M.C., Stüeken, E.E., Kipp, M.A., Buick, R., Knoll, A.H., 2017. Spatial and temporal
1095 trends in Precambrian nitrogen cycling: A Mesoproterozoic offshore nitrate minimum.
1096 *Geochimica et Cosmochimica Acta* 198, 315–337. <https://doi.org/10.1016/j.gca.2016.10.050>
- 1097 Konhauser, K.O., Lalonde, S.V., Planavsky, N.J., Pecoits, E., Lyons, T.W., Mojzsis, S.J.,
1098 Rouxel, O.J., Barley, M.E., Rosière, C., Fralick, P.W., Kump, L.R., Bekker, A., 2011.
1099 Aerobic bacterial pyrite oxidation and acid rock drainage during the Great Oxidation Event.
1100 *Nature* 478, 369–373. <https://doi.org/10.1038/nature10511>
- 1101 Kroopnick, P.M., 1985. The distribution of ¹³C of ΣCO₂ in the world oceans. *Deep Sea*
1102 *Research* 32, 57–84.
- 1103 Kroopnick, P.M., 1974. Correlations between ¹³C and ΣCO₂ in surface waters and
1104 atmospheric CO₂. *Earth and Planetary Science Letters* 22, 397–403.
- 1105 Kump, L.R., Junium, C., Arthur, M.A., Brasier, A., Fallick, A., Melezhik, V., Lepland, A.,
1106 Crne, A.E., Luo, G., 2011. Isotopic evidence for massive oxidation of organic matter
1107 following the Great Oxidation Event. *Science* 334, 1694–1696.
1108 <https://doi.org/10.1126/science.1213999>
- 1109 Latimer, J.C., Filippelli, G.M., 2001. Terrigenous input and paleoproductivity in the Southern
1110 Ocean. *Paleoceanography* 16, 627–643. <https://doi.org/10.1029/2000PA000586>

- 1111 Lehmann, M.F., Bernasconi, S.M., Barbieri, A., McKenzie, J.A., 2002. Preservation of
1112 organic matter and alteration of its carbon and nitrogen isotope composition during simulated
1113 and in situ early sedimentary diagenesis. *Geochimica et Cosmochimica Acta* 66, 3573–3584.
1114 [https://doi.org/10.1016/S0016-7037\(02\)00968-7](https://doi.org/10.1016/S0016-7037(02)00968-7)
- 1115 Lekele Baghekema, S.G., Lepot, K., Riboulleau, A., Fadel, A., Trentesaux, A., El Albani, A.,
1116 2017. Nanoscale analysis of preservation of *ca.* 2.1 Ga old Francevillian microfossils, Gabon.
1117 *Precambrian Research* 301, 1–18. <https://doi.org/10.1016/j.precamres.2017.08.024>
- 1118 Luo, G., Junium, C.K., Izon, G., Ono, S., Beukes, N.J., Algeo, T.J., Cui, Y., Xie, S.,
1119 Summons, R.E., 2018. Nitrogen fixation sustained productivity in the wake of the
1120 Palaeoproterozoic Great Oxygenation Event. *Nat Commun* 9, 978.
1121 <https://doi.org/10.1038/s41467-018-03361-2>
- 1122 Lyons, T.W., 1997. Sulfur isotopic trends and pathways of iron sulfide formation in upper
1123 Holocene sediments of the anoxic Black Sea. *Geochimica et Cosmochimica Acta* 61, 3367–
1124 3382. [https://doi.org/10.1016/S0016-7037\(97\)00174-9](https://doi.org/10.1016/S0016-7037(97)00174-9)
- 1125 Lyons, T.W., Reinhard, C.T., Planavsky, N.J., 2014. The rise of oxygen in Earth's early ocean
1126 and atmosphere. *Nature* 506, 307–315. <https://doi.org/10.1038/nature13068>
- 1127 Lyons, T.W., Severmann, S., 2006. A critical look at iron paleoredox proxies: New insights
1128 from modern euxinic marine basins. *Geochimica et Cosmochimica Acta* 70, 5698–5722.
1129 <https://doi.org/10.1016/j.gca.2006.08.021>
- 1130 Martin, A.P., Prave, A.R., Condon, D.J., Lepland, A., Fallick, A.E., Romashkin, A.E.,
1131 Medvedev, P.V., Rychanchik, D.V., 2015. Multiple Palaeoproterozoic carbon burial episodes
1132 and excursions. *Earth and Planetary Science Letters* 424, 226–236.
1133 <https://doi.org/10.1016/j.epsl.2015.05.023>
- 1134 Marty, B., Zimmermann, L., Pujol, M., Burgess, R., Philippot, P., 2013. Nitrogen Isotopic
1135 Composition and Density of the Archean Atmosphere. *Science* 342, 101–104.
1136 <https://doi.org/10.1126/science.1240971>
- 1137 Mayika, B.K., Moussavou, M., Prave, A.R., Lepland, A., Mbina, M., Kirsimäe, K., 2020. The
1138 Paleoproterozoic Francevillian succession of Gabon and the Lomagundi-Jatuli event. *Geology*
1139 48. <https://doi.org/10.1130/G47651.1>
- 1140 Melezhik, V.A., Fallick, A.E., Rychanchik, D.V., Kuznetsov, A.B., 2005. Palaeoproterozoic
1141 evaporites in Fennoscandia: Implications for seawater sulphate, the rise of atmospheric
1142 oxygen and local amplification of the $\delta^{13}\text{C}$ excursion. *Terra Nova* 17, 141–148.
1143 <https://doi.org/10.1111/j.1365-3121.2005.00600.x>
- 1144 Minagawa, M., Wada, E., 1986. Nitrogen isotope ratios of red tide organisms in the East
1145 China Sea: A characterization of biological nitrogen fixation. *Marine Chemistry* 19, 245–259.
1146 [https://doi.org/10.1016/0304-4203\(86\)90026-5](https://doi.org/10.1016/0304-4203(86)90026-5)
- 1147 Mouélé, I.M., Dudoignon, P., El Albani, A., Meunier, A., Boulvais, P., Gauthier-Lafaye, F.,
1148 Paquette, J.-L., Martin, H., Cuney, M., 2014. 2.9–1.9 Ga paleoalterations of Archean granitic
1149 basement of the Franceville basin (Gabon). *Journal of African Earth Sciences* 97, 244–260.
1150 <https://doi.org/10.1016/j.jafrearsci.2014.04.027>

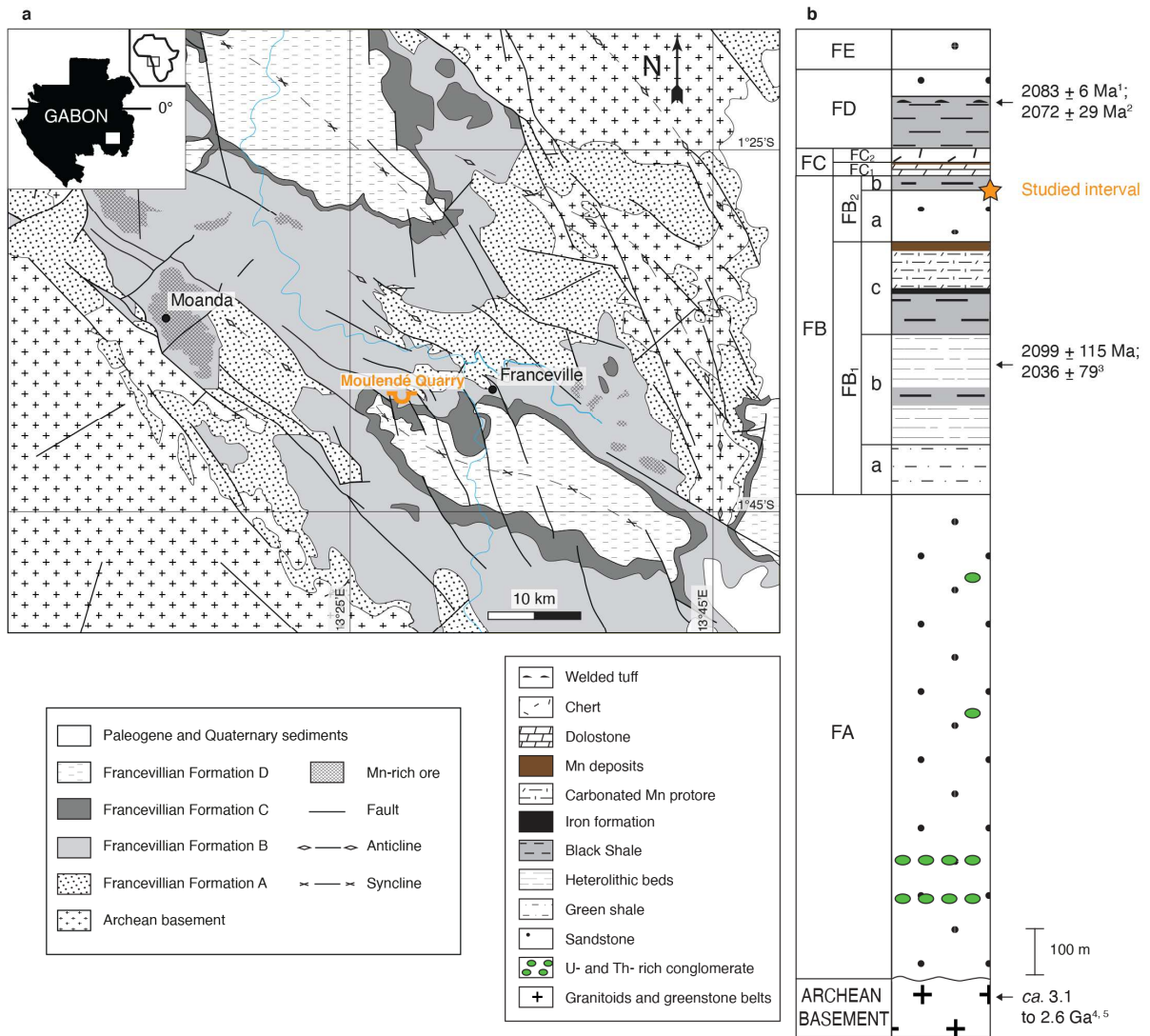
- 1151 Müller, P.J., 1977. C/N ratios in Pacific deep-sea sediments: Effect of inorganic ammonium
1152 and organic nitrogen compounds sorbed by clays. *Geochimica et Cosmochimica Acta* 41,
1153 765–776.
- 1154 Ngombi-Pemba, L., El Albani, A., Meunier, A., Grauby, O., Gauthier-Lafaye, F., 2014. From
1155 detrital heritage to diagenetic transformations, the message of clay minerals contained within
1156 shales of the Palaeoproterozoic Francevillian basin (Gabon). *Precambrian Research* 255, 63–
1157 76. <https://doi.org/10.1016/j.precamres.2014.09.016>
- 1158 Ossa Ossa, F., Eickmann, B., Hofmann, A., Planavsky, N.J., Asael, D., Pambo, F., Bekker,
1159 A., 2018. Two-step deoxygenation at the end of the Paleoproterozoic Lomagundi Event. *Earth
1160 and Planetary Science Letters* 486, 70–83. <https://doi.org/10.1016/j.epsl.2018.01.009>
- 1161 Ossa Ossa, F., Hofmann, A., Ballouard, C., Vorster, C., Schoenberg, R., Fiedrich, A.,
1162 Mayaga-Mikolo, F., Bekker, A., 2020. Constraining provenance for the uraniferous
1163 Paleoproterozoic Francevillian Group sediments (Gabon) with detrital zircon geochronology
1164 and geochemistry. *Precambrian Research* 343, 105724.
1165 <https://doi.org/10.1016/j.precamres.2020.105724>
- 1166 Papineau, D., Purohit, R., Goldberg, T., Pi, D., Shields, G.A., Bhu, H., Steele, A., Fogel,
1167 M.L., 2009. High primary productivity and nitrogen cycling after the Paleoproterozoic
1168 phosphogenic event in the Aravalli Supergroup, India. *Precambrian Research* 171, 37–56.
1169 <https://doi.org/10.1016/j.precamres.2009.03.005>
- 1170 Partin, C.A., Bekker, A., Planavsky, N.J., Lyons, T.W., 2015. Euxinic conditions recorded in
1171 the *ca.* 1.93 Ga Bravo Lake Formation, Nunavut (Canada): Implications for oceanic redox
1172 evolution. *Chemical Geology* 417, 148–162. <https://doi.org/10.1016/j.chemgeo.2015.09.004>
- 1173 Partin, C.A., Bekker, A., Planavsky, N.J., Scott, C.T., Gill, B.C., Li, C., Podkovyrov, V.,
1174 Maslov, A., Konhauser, K.O., Lalonde, S.V., Love, G.D., Poulton, S.W., Lyons, T.W., 2013.
1175 Large-scale fluctuations in Precambrian atmospheric and oceanic oxygen levels from the
1176 record of U in shales. *Earth and Planetary Science Letters* 369–370, 284–293.
1177 <https://doi.org/10.1016/j.epsl.2013.03.031>
- 1178 Pavlov, A.A., Kasting, J.F., 2002. Mass-independent fractionation of sulfur isotopes in
1179 Archean sediments: Strong evidence for an anoxic Archean atmosphere. *Astrobiology* 2, 27–
1180 41. <https://doi.org/10.1089/153110702753621321>
- 1181 Planavsky, N.J., Bekker, A., Hofmann, A., Owens, J.D., Lyons, T.W., 2012. Sulfur record of
1182 rising and falling marine oxygen and sulfate levels during the Lomagundi event. *Proceedings
1183 of the National Academy of Sciences* 109, 18300–18305.
- 1184 Planavsky, N.J., McGoldrick, P., Scott, C.T., Li, C., Reinhard, C.T., Kelly, A.E., Chu, X.,
1185 Bekker, A., Love, G.D., Lyons, T.W., 2011. Widespread iron-rich conditions in the mid-
1186 Proterozoic ocean. *Nature* 477, 448–451. <https://doi.org/10.1038/nature10327>
- 1187 Poulton, S.W., Canfield, D.E., 2011. Ferruginous conditions: A dominant feature of the ocean
1188 through Earth's history. *Elements* 7, 107–112. <https://doi.org/10.2113/gselements.7.2.107>
- 1189 Poulton, S.W., Canfield, D.E., 2005. Development of a sequential extraction procedure for
1190 iron: Implications for iron partitioning in continentally derived particulates. *Chemical
1191 Geology* 214, 209–221. <https://doi.org/10.1016/j.chemgeo.2004.09.003>

- 1192 Poulton, S.W., Fralick, P.W., Canfield, D.E., 2010. Spatial variability in oceanic redox
1193 structure 1.8 billion years ago. *Nature Geosci* 3, 486–490. <https://doi.org/10.1038/ngeo889>
- 1194 Poulton, S.W., Raiswell, R., 2002. The low-temperature geochemical cycle of iron: From
1195 continental fluxes to marine sediment deposition. *American Journal of Science* 302, 774–805.
1196 <https://doi.org/10.2475/ajs.302.9.774>
- 1197 Pr eat, A., Bouton, P., Thi blemont, D., Prian, J.-P., Ndounze, S.S., Delpomdor, F., 2011.
1198 Paleoproterozoic high $\delta^{13}\text{C}$ dolomites from the Lastoursville and Franceville basins (SE
1199 Gabon): Stratigraphic and synsedimentary subsidence implications. *Precambrian Research*
1200 189, 212–228. <https://doi.org/10.1016/j.precamres.2011.05.013>
- 1201 Raiswell, R., Hardisty, D.S., Lyons, T.W., Canfield, D.E., Owens, J.D., Planavsky, N.J.,
1202 Poulton, S.W., Reinhard, C.T., 2018. The iron paleoredox proxies: A guide to the pitfalls,
1203 problems and proper practice. *Am J Sci* 318, 491–526. <https://doi.org/10.2475/05.2018.03>
- 1204 Raiswell, R., Newton, R., Bottrell, S.H., Coburn, P.M., Briggs, D.E.G., Bond, D.P.G.,
1205 Poulton, S.W., 2008. Turbidite depositional influences on the diagenesis of Beecher’s trilobite
1206 bed and the hunsr uck slate; sites of soft tissue pyritization. *American Journal of Science* 308,
1207 105–129. <https://doi.org/10.2475/02.2008.01>
- 1208 Rasmussen, B., Buick, R., 1999. Redox state of the Archean atmosphere: Evidence from
1209 detrital heavy minerals in ca. 3250–2750 Ma sandstones from the Pilbara craton, Australia.
1210 *Geology* 27, 115–118.
- 1211 Redfield, A.C., 1958. The biological control of chemical factors in the environment.
1212 *American Scientist* 46, 230A, 205–221.
- 1213 Reinhard, C.T., Planavsky, N.J., Gill, B.C., Ozaki, K., Robbins, L.J., Lyons, T.W., Fischer,
1214 W.W., Wang, C., Cole, D.B., Konhauser, K.O., 2017. Evolution of the global phosphorus
1215 cycle. *Nature* 541, 386–389. <https://doi.org/10.1038/nature20772>
- 1216 Reinhard, C.T., Planavsky, N.J., Robbins, L.J., Partin, C.A., Gill, B.C., Lalonde, S.V.,
1217 Bekker, A., Konhauser, K.O., Lyons, T.W., 2013. Proterozoic ocean redox and
1218 biogeochemical stasis. *Proceedings of the National Academy of Sciences* 110, 5357–5362.
1219 <https://doi.org/10.1073/pnas.1208622110>
- 1220 Reynaud, J.-Y., Trentesaux, A., El Albani, A., Aubineau, J., Ngombi-Pemba, L., Guiyeligou,
1221 G., Bouton, P., Gauthier-Lafaye, F., Weber, F., 2017. Depositional setting of the 2.1 Ga
1222 Francevillian macrobiota (Gabon): Rapid mud settling in a shallow basin swept by high-
1223 density sand flows. *Sedimentology* 65, 670–701.
- 1224 Robinson, R.S., Kienast, M., Luiza Albuquerque, A., Altabet, M., Contreras, S., De Pol Holz,
1225 R., Dubois, N., Francois, R., Galbraith, E., Hsu, T.-C., Ivanochko, T., Jaccard, S., Kao, S.-J.,
1226 Kiefer, T., Kienast, S., Lehmann, M., Martinez, P., McCarthy, M., M obius, J., Pedersen, T.,
1227 Quan, T.M., Ryabenko, E., Schmittner, A., Schneider, R., Schneider-Mor, A., Shigemitsu, M.,
1228 Sinclair, D., Somes, C., Studer, A., Thunell, R., Yang, J.-Y., 2012. A review of nitrogen
1229 isotopic alteration in marine sediments. *Paleoceanography* 27, PA4203.
1230 <https://doi.org/10.1029/2012PA002321>
- 1231 Rudnick, R.L., Gao, S., 2003. Composition of the Continental Crust, in: Rudnick, R.L. (Ed.),
1232 *The Crust*. Elsevier-Pergamon, Oxford, pp. 1–64.

- 1233 Sano, Y., Pillinger, C.T., 1990. Nitrogen isotopes and N₂/Ar ratios in cherts: An attempt to
1234 measure time evolution of atmospheric ⁶15N value. *Geochemical Journal* 24, 315–325.
- 1235 Schidlowski, M., 1987. Application of stable carbon isotopes to early biochemical evolution
1236 on Earth. *Annual Review of Earth Planetary Sciences* 15, 47–72.
- 1237 Schröder, S., Bekker, A., Beukes, N.J., Strauss, H., van Niekerk, H.S., 2008. Rise in seawater
1238 sulphate concentration associated with the Paleoproterozoic positive carbon isotope
1239 excursion: Evidence from sulphate evaporites in the ~2.2–2.1 Gyr shallow-marine Lucknow
1240 Formation, South Africa. *Terra Nova* 20, 108–117. <https://doi.org/10.1111/j.1365-3121.2008.00795.x>
- 1242 Schroeder, P.A., McLain, A.A., 1998. Illite-smectites and the influence of burial diagenesis
1243 on the geochemical cycling of nitrogen. *Clay Minerals* 33, 539–546.
1244 <https://doi.org/10.1180/000985598545877>
- 1245 Scott, C., Lyons, T.W., 2012. Contrasting molybdenum cycling and isotopic properties in
1246 euxinic versus non-euxinic sediments and sedimentary rocks: Refining the paleoproxies.
1247 *Chemical Geology* 324–325, 19–27. <https://doi.org/10.1016/j.chemgeo.2012.05.012>
- 1248 Scott, C., Lyons, T.W., Bekker, A., Shen, Y., Poulton, S.W., Chu, X., Anbar, A.D., 2008.
1249 Tracing the stepwise oxygenation of the Proterozoic ocean. *Nature* 452, 456–459.
1250 <https://doi.org/10.1038/nature06811>
- 1251 Sigman, D.M., Karsh, K.L., Casciotti, K.L., 2009. Ocean process tracers: Nitrogen isotopes
1252 in the ocean, in: Steele, J.H., Turekian, K., Thorpe, S. (Eds.), *Encyclopedia of Ocean
1253 Sciences*. Academic, London, pp. 40–54.
- 1254 Slotznick, S.P., Eiler, J.M., Fischer, W.W., 2018. The effects of metamorphism on iron
1255 mineralogy and the iron speciation redox proxy. *Geochimica et Cosmochimica Acta* 224, 96–
1256 115.
- 1257 Smittenberg, R.H., Pancost, R.D., Hopmans, E.C., Paetzel, M., Sinninghe Damsté, J.S., 2004.
1258 A 400-year record of environmental change in an euxinic fjord as revealed by the sedimentary
1259 biomarker record. *Palaeogeography, Palaeoclimatology, Palaeoecology* 202, 331–351.
1260 [https://doi.org/10.1016/S0031-0182\(03\)00642-4](https://doi.org/10.1016/S0031-0182(03)00642-4)
- 1261 Sohm, J.A., Webb, E.A., Capone, D.G., 2011. Emerging patterns of marine nitrogen fixation.
1262 *Nat Rev Microbiol* 9, 499–508. <https://doi.org/10.1038/nrmicro2594>
- 1263 Sperling, E.A., Halverson, G.P., Knoll, A.H., Macdonald, F.A., Johnston, D.T., 2013. A basin
1264 redox transect at the dawn of animal life. *Earth and Planetary Science Letters* 371–372, 143–
1265 155. <https://doi.org/10.1016/j.epsl.2013.04.003>
- 1266 Stüeken, E.E., 2013. A test of the nitrogen-limitation hypothesis for retarded eukaryote
1267 radiation: Nitrogen isotopes across a Mesoproterozoic basinal profile. *Geochimica et
1268 Cosmochimica Acta* 120, 121–139. <https://doi.org/10.1016/j.gca.2013.06.002>
- 1269 Stüeken, E.E., Buick, R., Guy, B.M., Koehler, M.C., 2015. Isotopic evidence for biological
1270 nitrogen fixation by molybdenum-nitrogenase from 3.2 Gyr. *Nature* 520, 666–669.
1271 <https://doi.org/10.1038/nature14180>
- 1272 Stüeken, E.E., Kipp, M.A., Koehler, M.C., Buick, R., 2016. The evolution of Earth's

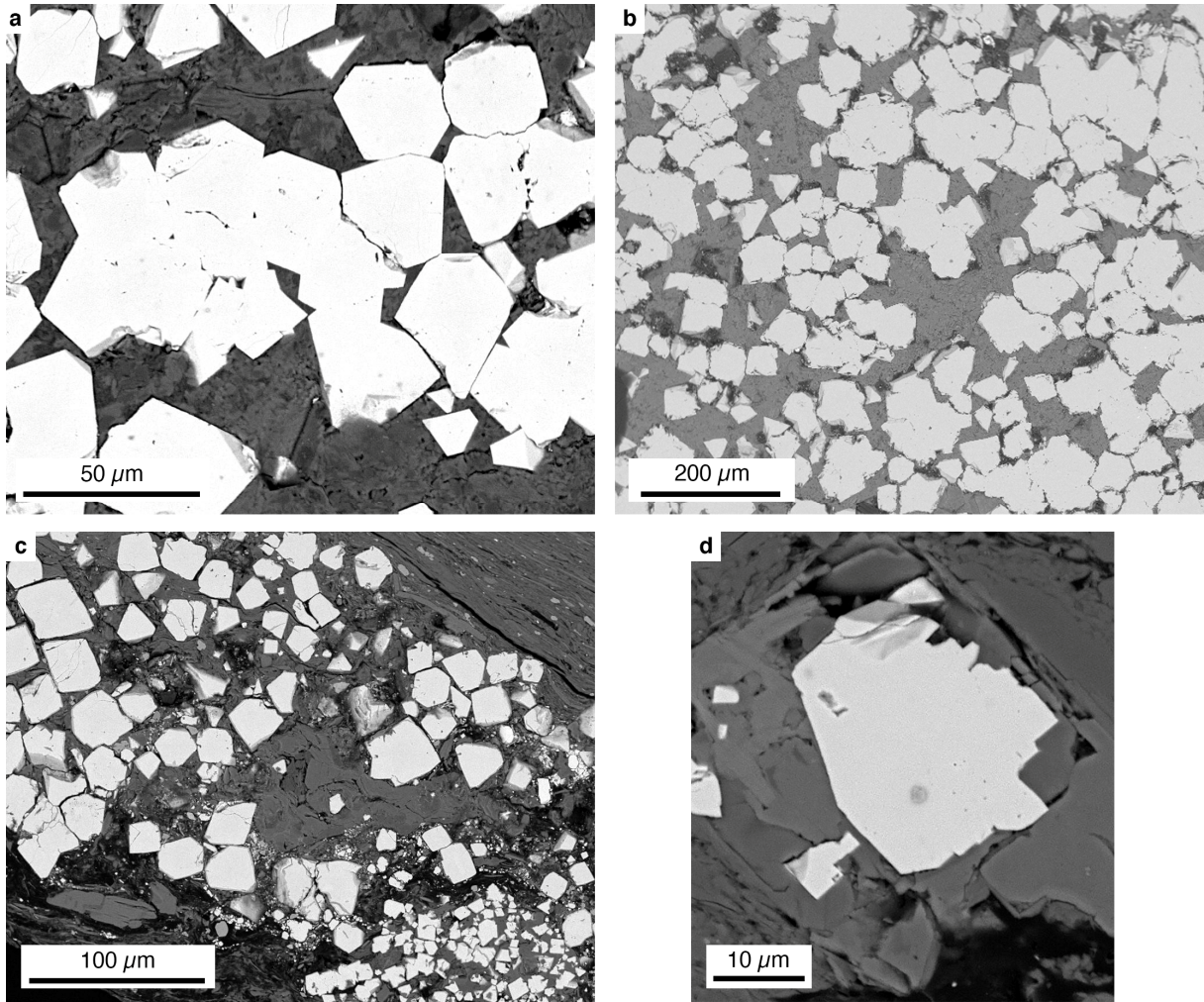
- 1273 biogeochemical nitrogen cycle. *Earth-Science Reviews* 160, 220–239.
1274 <https://doi.org/10.1016/j.earscirev.2016.07.007>
- 1275 Stüeken, E.E., Zaloumis, J., Meixnerová, J., Buick, R., 2017a. Differential metamorphic
1276 effects on nitrogen isotopes in kerogen extracts and bulk rocks. *Geochimica et Cosmochimica*
1277 *Acta* 217, 80–94. <https://doi.org/10.1016/j.gca.2017.08.019>
- 1278 Stüeken, E.E., Buick, R., Anderson, R.E., Baross, J.A., Planavsky, N.J., Lyons, T.W., 2017b.
1279 Environmental niches and metabolic diversity in Neoproterozoic lakes. *Geobiology* 15, 767–783.
1280 <https://doi.org/10.1111/gbi.12251>
- 1281 Suarez, C., Piculell, M., Modin, O., Langenheder, S., Persson, F., Hermansson, M., 2019.
1282 Thickness determines microbial community structure and function in nitrifying biofilms via
1283 deterministic assembly. *Scientific Reports* 9, 5110. [https://doi.org/10.1038/s41598-019-](https://doi.org/10.1038/s41598-019-41542-1)
1284 [41542-1](https://doi.org/10.1038/s41598-019-41542-1)
- 1285 Tesdal, J.-E., Galbraith, E.D., Kienast, M., 2013. Nitrogen isotopes in bulk marine sediment:
1286 linking seafloor observations with subseafloor records. *Biogeosciences* 10, 101–118.
1287 <https://doi.org/10.5194/bg-10-101-2013>
- 1288 Thiéblemont, D., Bouton, P., Prétat, A., Goujou, J.-C., Tegye, M., Weber, F., Ebang Obiang,
1289 M., Joron, J.L., Treuil, M., 2014. Transition from alkaline to calc-alkaline volcanism during
1290 evolution of the Paleoproterozoic Francevillian basin of eastern Gabon (Western Central
1291 Africa). *Journal of African Earth Sciences* 99, 215–227.
1292 <https://doi.org/10.1016/j.jafrearsci.2013.12.007>
- 1293 Thiéblemont, D., Castaing, C., Billa, M., Bouton, P., Prétat, A., 2009. Notice explicative de la
1294 carte géologique et des ressources minérales de la République gabonaise à 1/1,000,000.
- 1295 Thunell, R.C., Sigman, D.M., Muller-Karger, F., Astor, Y., Varela, R., 2004. Nitrogen isotope
1296 dynamics of the Cariaco Basin, Venezuela. *Global Biogeochem. Cycles* 18, GB3001.
1297 <https://doi.org/10.1029/2003GB002185>
- 1298 Tribouillard, N., Algeo, T.J., Lyons, T., Riboulleau, A., 2006. Trace metals as paleoredox and
1299 paleoproductivity proxies: An update. *Chemical Geology* 232, 12–32.
1300 <https://doi.org/10.1016/j.chemgeo.2006.02.012>
- 1301 Tribouillard, N., Bout-Roumazielles, V., Algeo, T., Lyons, T.W., Sionneau, T., Montero-
1302 Serrano, J.C., Riboulleau, A., Baudin, F., 2008. Paleodepositional conditions in the Orca
1303 Basin as inferred from organic matter and trace metal contents. *Marine Geology* 254, 62–72.
1304 <https://doi.org/10.1016/j.margeo.2008.04.016>
- 1305 Tyrrell, T., 1999. The relative influences of nitrogen and phosphorus on oceanic primary
1306 production. *Nature* 400, 525–531.
- 1307 Wang, D., Ling, H.-F., Struck, U., Zhu, X.-K., Zhu, M., He, T., Yang, B., Gamper, A.,
1308 Shields, G.A., 2018. Coupling of ocean redox and animal evolution during the Ediacaran-
1309 Cambrian transition. *Nat Commun* 9, 2575. <https://doi.org/10.1038/s41467-018-04980-5>
- 1310 Wang, X., Shi, X., Tang, D., Zhang, W., 2013. Nitrogen isotope evidence for redox variations
1311 at the Ediacaran-Cambrian transition in South China. *The Journal of Geology* 121, 489–502.
1312 <https://doi.org/10.1086/671396>

- 1313 Wang, X., Zhang, S., Wang, H., Bjerrum, C.J., Hammarlund, E.U., Haxen, E.R., Su, J.,
1314 Wang, Y., Canfield, D.E., 2017. Oxygen, climate and the chemical evolution of a 1400
1315 million year old tropical marine setting. *Am J Sci* 317, 861–900.
1316 <https://doi.org/10.2475/08.2017.01>
- 1317 Warke, M.R., Di Rocco, T., Zerkle, A.L., Lepland, A., Prave, A.R., Martin, A.P., Ueno, Y.,
1318 Condon, D.J., Claire, M.W., 2020. The Great Oxidation Event preceded a Paleoproterozoic
1319 “snowball Earth.” *Proc Natl Acad Sci USA* 117, 13314–13320.
1320 <https://doi.org/10.1073/pnas.2003090117>
- 1321 Weber, F., 1968. Une série précambrienne du Gabon : le Francevillien. *Sédimentologie,*
1322 *géochimie, relations avec les gîtes minéraux associés.* Université de Strasbourg, Strasbourg.
- 1323 Williams, L.B., Ferrell Jr, R.E., 1991. Ammonium substitution in illite during maturation of
1324 organic Mmatter. *Clays and Clay Minerals* 39, 400–408.
1325 <https://doi.org/10.1346/CCMN.1991.0390409>
- 1326 Williams, L.B., Ferrell Jr, R.E., Hutcheon, I., Bakel, A.J., Walsh, M.M., Krouse, H.R., 1995.
1327 Nitrogen isotope geochemistry of organic matter and minerals during diagenesis and
1328 hydrocarbon migration. *Geochimica et Cosmochimica Acta* 59, 765–779.
1329 [https://doi.org/10.1016/0016-7037\(95\)00005-K](https://doi.org/10.1016/0016-7037(95)00005-K)
- 1330 Williams, R.J.P., Fraústo da Silva, J.J.R., 2002. The Involvement of Molybdenum in Life.
1331 *Biochemical and Biophysical Research Communications* 292, 293–299.
1332 <https://doi.org/10.1006/bbrc.2002.6518>
- 1333 Woebken, D., Burow, L.C., Behnam, F., Mayali, X., Schintlmeister, A., Fleming, E.D.,
1334 Prufert-Bebout, L., Singer, S.W., López Cortés, A., Hoehler, T.M., Pett-Ridge, J., Spormann,
1335 A.M., Wagner, M., Weber, P.K., Bebout, B.M., 2015. Revisiting N₂ fixation in Guerrero
1336 Negro intertidal microbial mats with a functional single-cell approach. *ISME J* 9, 485–496.
1337 <https://doi.org/10.1038/ismej.2014.144>
- 1338 Zerkle, A.L., House, C.H., Brantley, S.L., 2005. Biogeochemical signatures through time as
1339 inferred from whole microbial genomes. *American Journal of Science* 305, 467–502.
1340 <https://doi.org/10.2475/ajs.305.6-8.467>
- 1341 Zerkle, A.L., Junium, C.K., Canfield, D.E., House, C.H., 2008. Production of ¹⁵N-depleted
1342 biomass during cyanobacterial N₂-fixation at high Fe concentrations. *Journal of Geophysical*
1343 *Research* 113, G03014. <https://doi.org/10.1029/2007JG000651>
- 1344 Zerkle, A.L., Poulton, S.W., Newton, R.J., Mettam, C., Claire, M.W., Bekker, A., Junium,
1345 C.K., 2017. Onset of the aerobic nitrogen cycle during the Great Oxidation Event. *Nature* 542,
1346 465–467. <https://doi.org/10.1038/nature20826>
- 1347 Zhang, X., Sigman, D.M., Morel, F.M.M., Kraepiel, A.M.L., 2014. Nitrogen isotope
1348 fractionation by alternative nitrogenases and past ocean anoxia. *Proceedings of the National*
1349 *Academy of Sciences* 111, 4782–4787. <https://doi.org/10.1073/pnas.1402976111>
- 1350



1352

1353 **Figure 1:** Geological map of the Paleoproterozoic Franceville sub-basin modified from
 1354 Bouton et al. (2009b) **(a)** and general lithostratigraphic column of the Francevillian Group **(b)**.
 1355 The Moulendé Quarry is the studied area. Sources of ages: ¹ - Horie *et al.* (2005); ² -
 1356 Thiéblemont *et al.* (2009); ³ - Bros *et al.* (1992); ⁴ - Mouélé *et al.* (2014); ⁵ - Ossa Ossa *et al.*
 1357 (2020). The figure is modified from Aubineau *et al.* (2020).



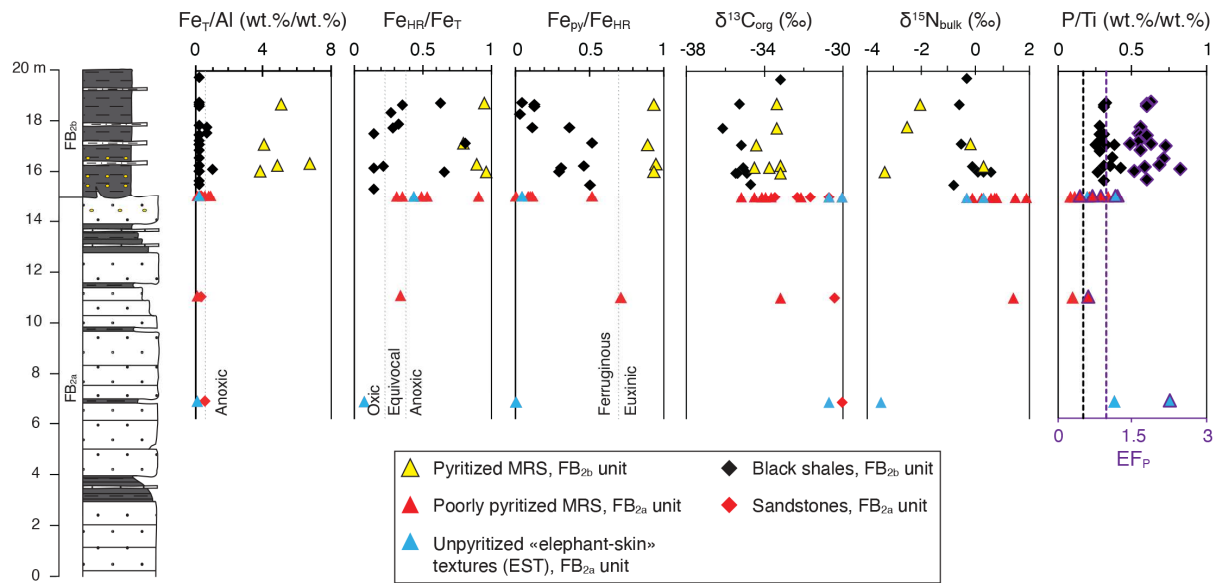
1358

1359

1360

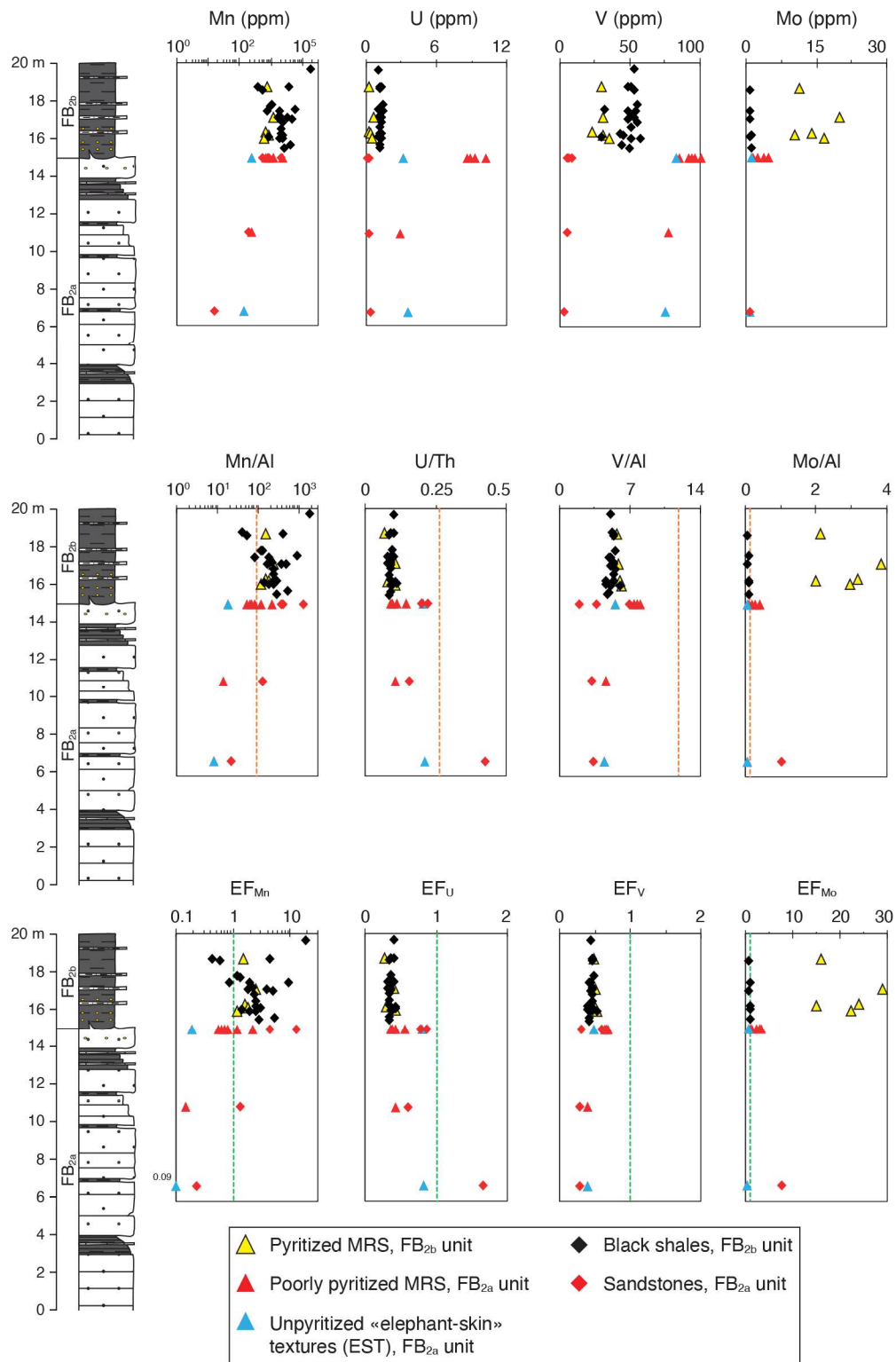
1361

Figure 2: SEM images in backscatter mode of pyrite crystals showing the absence of alteration and recrystallization. **a** and **b**, Pyritized MRS. **c**, Poorly pyritized MRS. **d**, Black shales.



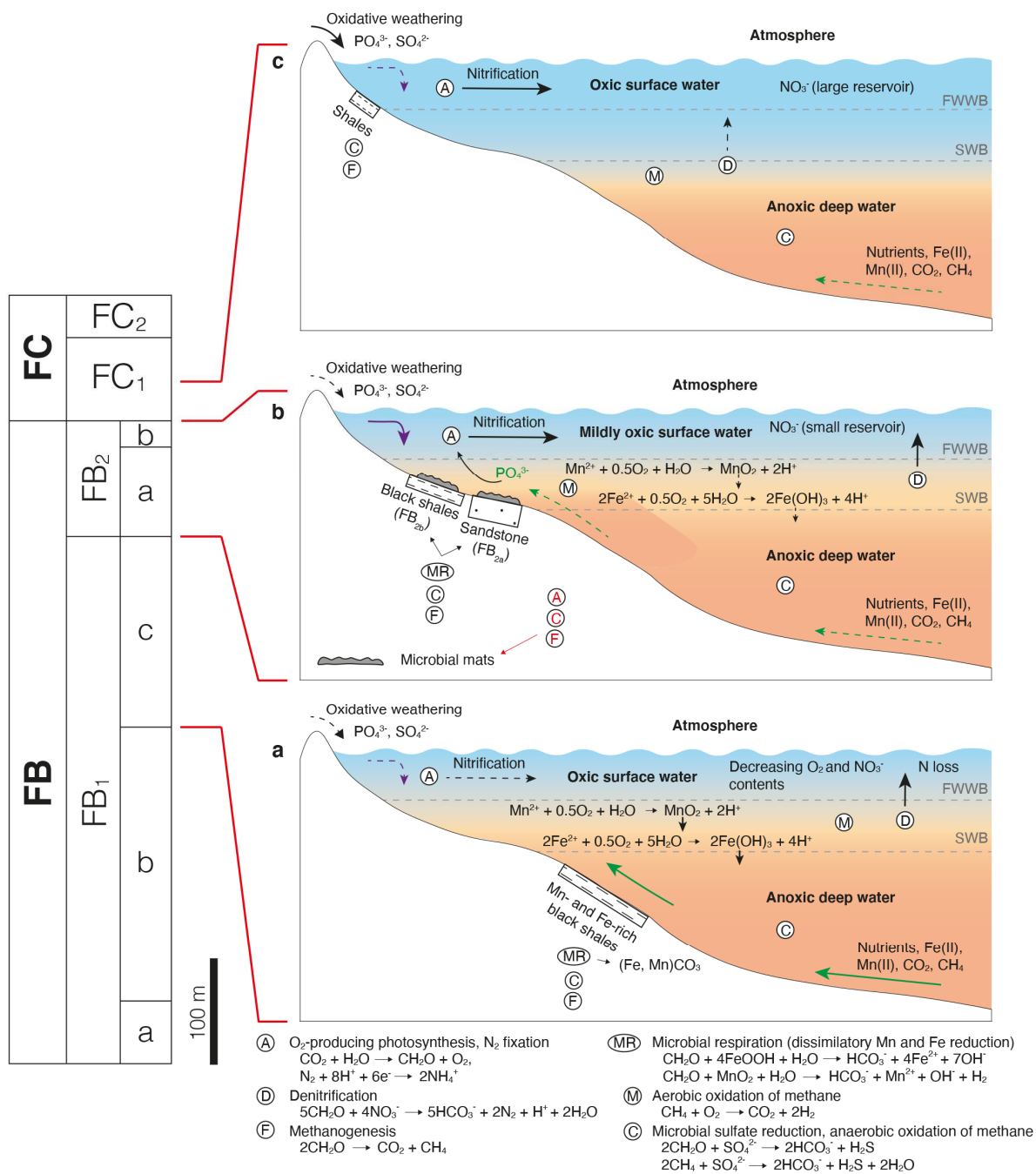
1362

1363 **Figure 3:** Geochemical data for the MRS and host sediments plotted along the
 1364 lithostratigraphic profile of the studied sequence of the FB₂ Member. Grey, black, and purple
 1365 vertical lines represent redox boundaries as in Raiswell *et al.* (2018), the UCC value from
 1366 Rudnick & Gao (2003), and the EF_P for the UCC is 1, respectively. Fe/Al for the UCC is
 1367 shown with grey dash line.



1368

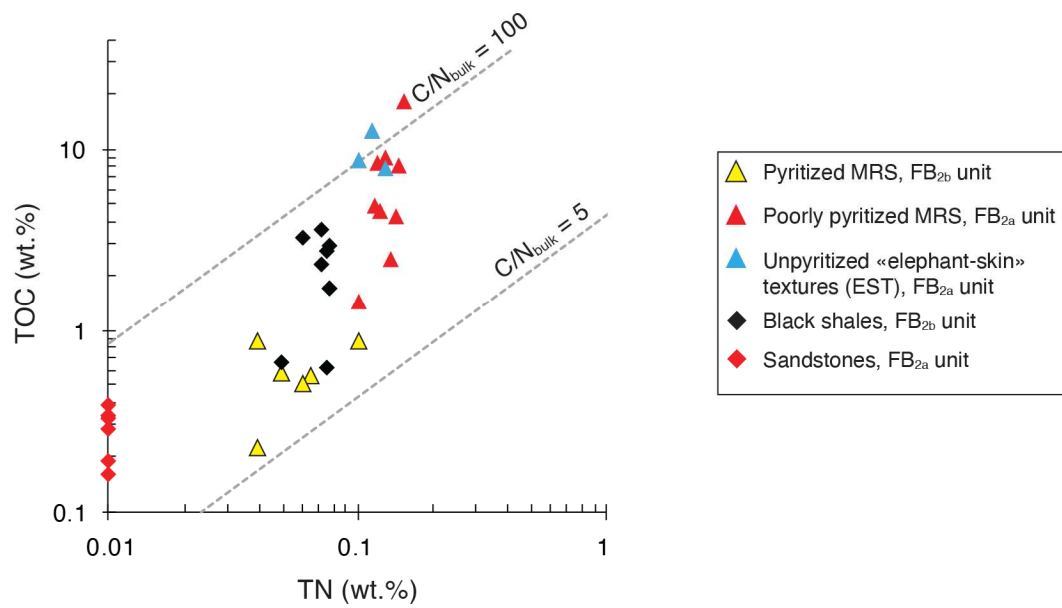
1369 **Figure 4:** Data for redox-sensitive metals from the MRS and host sediments plotted along
 1370 the lithostratigraphic profile of the studied sequence of the FB₂ Member. Orange and green
 1371 vertical lines correspond to the UCC ratio from Rudnick & Gao (2003) and the EF for the
 1372 UCC of 1, respectively. The Mn/Al, V/Al, and Mo/Al ratios are expressed in ppm/wt.%.



1373

1374 **Figure 5:** Proposed reconstruction of redox conditions during deposition of the Upper
 1375 Francevillian Group at the end of the LE. **a** - During deposition of the upper part of the FB₁
 1376 Member, upwelling of reducing fluids into oxic, shallow coastal area (Ossa Ossa et al., 2018)
 1377 likely led to the first step of deoxygenation and decrease in bioavailable nitrate. **b** - During
 1378 deposition of the FB₂ Member, bioavailable nitrate was scarce. Upwelling brought anoxic
 1379 bottom seawater rich in Fe, Mn, and P. Phosphorous availability in surface waters along with
 1380 limitation of bioavailable nitrate resulted in high primary productivity fueled by diazotrophs,
 1381 which partially replenished bioavailable nitrogen. Microbial mats flourished and also fixed
 1382 nitrogen. Sandstones were delivered with high-density gravity currents to the mud-rich

1383 depositional environment (Reynaud et al., 2017). The FB₂ Member is, therefore, interpreted
1384 as a forced regressive system tract. **c** - Recovery in nitrate availability during deposition of
1385 the lower part of FC₁ Member (cf. Kipp *et al.*, 2018) indicates the transient nature of nitrate
1386 limitation during deposition of the FB₂ Member that was modulated by the redox structure of
1387 the Francevillian basin, degree of isolation from the ocean, and flux of reductants. FWWB,
1388 fair-weather wave base; SWB, storm wave base. Purple and green arrows indicate the
1389 sediment supply and the upwelling system, respectively. Processes were less intense when
1390 arrows are dotted.



1391

1392 **Figure 6:** Cross plot of total organic carbon versus total nitrogen for MRS and host
 1393 sediments. Dotted lines show molar C:N ratios of 5 and 100. The molar C:N values of
 1394 modern marine phytoplankton range from 4 to 10 (Ader et al., 2016; Canfield et al., 2010).
 1395 Remineralization of biomass in the water column and during diagenesis increases the C:N
 1396 ratios.